



Experimental investigation of a point-absorber wave energy converter response in different wave-type representations of extreme sea states[☆]

Zahra Shahroozi^{a,*}, Malin Göteman^{a,b}, Jens Engström^a

^a Department of Electrical Engineering, Uppsala University, Ångströmlaboratoriet, Lägerhyddsvägen 1, 752 37 Uppsala, Sweden

^b Centre of Natural Hazards and Disaster Science (CNDS), Villavägen 16, 752 36 Uppsala, Sweden

ARTICLE INFO

Keywords:

Extreme waves
Wave breaking
Slamming
Overtopping
Wave types
End-stop
PTO damping

ABSTRACT

The experimental results of a 1:30 scaled wave tank experiment of a point-absorber in extreme sea states and intermediate water depth are studied. The effect of the PTO damping parameter and different non-linear phenomena in extreme wave conditions such as wave breaking and overtopping are investigated with the focus on the maximum line (mooring) force in the presence of an upper end-stop. In the comparison of different wave-type representations, i.e. irregular, regular, and focused waves, of the same sea state, not all the wave types necessarily yield to the same peak line force. Moreover, there exists an optimum damping value for each sea state in which the smallest peak force is achieved. Both end-stop spring compression and wave breaking slamming result in peak line forces which may be compensated by overtopping water pressure. Large surge motion is obtained for waves with a long wavelength which can contribute to higher and more damaging line forces.

1. Introduction

For studying the survivability of wave energy converters (WECs), the dynamics of the forces exerted on the system must be well understood. Extreme waves imply steep waves with strong non-linear phenomena such as wave breaking (Saincher and Banerjee, 2016), slamming (Wang and Soares, 2017), and overtopping (Kofoed, 2002).

Many authors have addressed the effect of extreme waves on WEC systems either by means of numerical or experimental analysis. Göteman et al. (2015) and Sjökvist et al. (2017) found that increasing the friction damping results in lower peak forces for WECs subjected to extreme waves. Göteman et al. conducted a 1:20 scaled wave tank experiment with a linear friction power take-off (PTO), and three different buoy shapes in extreme waves considering both irregular and focused waves. Later Sjökvist et al. confirmed their computational fluid dynamics (CFD), with the physical experiment by Göteman et al.. Hann et al. (2015) studied both the effect of wave steepness using non-breaking focused waves and breaking location using plunging breaking waves on a taut moored floating body through the experimental measurement with a 1:50 scaled model. They noticed that the magnitude of the mooring load was greatly influenced by the wave breaking location rather than wave steepness. In Roper-Giralda et al. (2020), the horizontal and vertical forces on a heaving point-absorber were studied

using the Smoothed Particle Hydrodynamics (SPH) method. They also made a comparison between numerical and 1:10 scaled experimental results for regular waves. In their study of the survivability for the focused waves, they concluded that submerging the heaving buoy at a certain depth decreases the loads on the structure. Katsidoniotaki et al. (2020) investigated the line force on a point-absorbing device exposed to extreme sea states from the Dowsing site with a 50-year return period through CFD simulation. They evaluated the effect of wave breaking, slamming, and steepness for focused waves and observed that high waves contribute to high loads.

Despite the advanced numerical simulations, capturing the non-linearities without over- or underestimation of these effects is rather challenging. Experimental wave tank tests are useful tools to profoundly comprehend the influence of non-linearities and validate numerical simulations. Coe et al. (2014) presented a review of the methods to model the WECs in extreme sea states both physically and numerically, i.e. covering low and high-fidelity methods.

This paper investigates the dynamics of a point-absorbing WEC in extreme wave conditions for sea states with a 50-year return period for the Dowsing site, North Sea. For this purpose, a small scale 1:30 wave tank experiment is conducted consisting of a linear friction PTO and a buoy with an ellipsoidal bottom. The main contributions of this work

[☆] This research is supported by the Swedish Energy Agency (project number 47264-1), the Swedish Research Council (grant number 2020-03634), Centre of Natural Hazards and Disaster Science (CNDS), and StandUp for Energy.

* Corresponding author.

E-mail address: zahra.shahroozi@angstrom.uu.se (Z. Shahroozi).

<https://doi.org/10.1016/j.oceaneng.2022.110693>

Received 26 July 2021; Received in revised form 10 January 2022; Accepted 22 January 2022

Available online 12 February 2022

0029-8018/© 2022 The Authors. Published by Elsevier Ltd. This is an open access article under the CC BY license (<http://creativecommons.org/licenses/by/4.0/>).

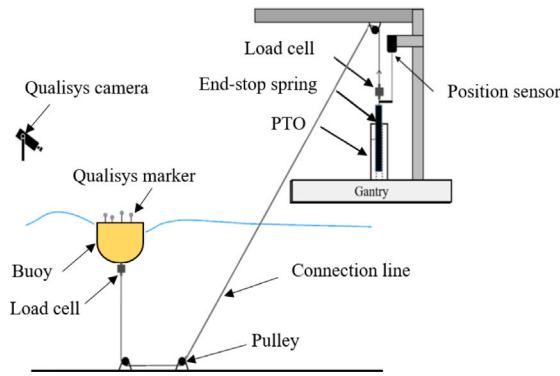


Fig. 1. The sketch of the wave tank experiment, retrieved from Shahroozi (2021).

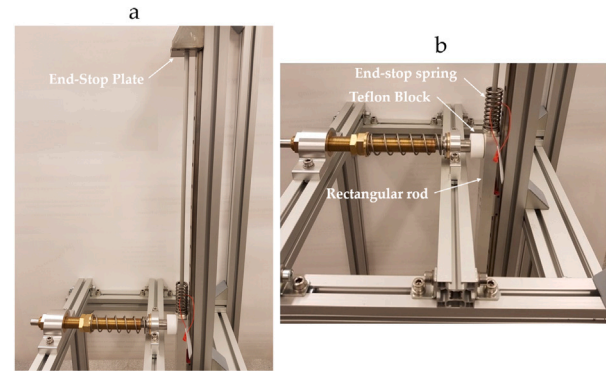


Fig. 2. Linear friction-based PTO for PTO damping D_1 and D_2 photo where a , and b are shown side and top views, respectively. Sub-figure b is retrieved from Shahroozi et al. (2021).

can be listed as: studying whether different wave-type representations (regular, focused, and irregular waves) of the same sea state result in the same maximum line force; and, evaluating how different damping cases from the lower bound, i.e. zero PTO damping, to the higher bound, i.e. locked PTO, would influence the line force; also, examining the inclusion of an end-stop spring in extreme events; and finally, assessing the line force for the sea states with the wave frequency around the natural frequency of the system in heave. Moreover, the consequences of different non-linear phenomena such as wave breaking, slamming, and overtopping in extreme waves are explored.

The remainder of this paper is as follows: in Section 2, the experimental setup and waves' calibration are explained. Moreover, the background to theory and analysis of the extreme waves' phenomena is provided. The results of the effect of different wave types, significant wave height, peak period, damping cases, as well as the effect of the wave breaking and steepness, end-stop spring compression, slamming, overtopping, and natural frequency are elaborated in Section 4. The discussion on the findings of the results is given in Section 5, and lastly, the conclusions of the work are summarized in Section 6.

2. Methodology

2.1. Experimental setup

In this section, the wave tank experiment scale 1:30 conducted in the Ocean and Coastal Engineering Laboratory of Aalborg University is described. The experimental setup is depicted in Fig. 1. The wave tank experiment is scaled based on the full-scale Uppsala University WEC. Using the Froude-scaling law, the scaled parameters are acquired. The choice of the 1:30 scale is a compromise between a large enough scale to model a realistic system, and a small enough scale to be able to generate extreme waves from North sea wave climate in the wave tank.

2.1.1. Power take-off and end-stop

In this experiment, a 1:30 scaled friction damping linear power take-off (PTO) is designed and used, see Fig. 2. This PTO consists of a rod connected to a linear guide for providing a smooth and robust movement with minimal vibration, a spring-Teflon module for applying a constant friction damping force, and an end-stop spring. In total, four PTO damping configurations are tested that are D_0 , D_1 , D_2 , and D_∞ for which the friction damping forces are: $F_{D_0} \approx 0$ N, $F_{D_1} \approx 7.4$ N, $F_{D_2} \approx 18.9$ N. The locked PTO represents the infinite damping coefficient case. In other words, considering equivalent viscous damping (Balachandran and Magrab, 2018) for the PTO, when the damping coefficient goes to infinity, the PTO becomes practically locked. Hence, by locking the PTO at the equilibrium position, the infinite damping coefficient is achieved. For damping configurations D_0 and D_∞ , the linear guide is removed

and replaced by a rod and attached weights equivalent to the mass of the PTO. In the zero damping case, the rod is free to move while in the D_∞ case, the rod is restrained from any movement. Note that the damping configurations discussed throughout the paper refer to the PTO damping cases. The PTO mass, which includes the translator mass and all the attached equipment such as loop, turnbuckle, and load cell, is 2.138 ± 0.001 kg.

In this setup, the translator motion is constrained only by an upper end-stop and no lower end-stop exists. The end-stop spring with a coefficient of 5.9 N/mm is used whose uncompressed and compressed lengths are 60 mm and 28 mm, respectively. To capture the full end-stop spring compression effect, a stroke length of 220 mm is considered.

2.1.2. Buoy

A 1:30 scaled cylindrical buoy with an ellipsoidal bottom made of aluminum with a height of 380 mm and a diameter of 330 mm is built, see Fig. 3. The buoy's mass is 15.73 ± 0.001 kg with a 230 mm draft. The center of gravity is $x_{CG} = 0.0$ mm, $y_{CG} = 0.0$ mm, and $z_{CG} = 118.6$ mm with respect to the origin located at the bottom center of the buoy with the z -axis pointing in the upright direction. The moments of inertia with respect to a coordinate system with the same orientation but located at CG are $I_{xx} = 0.3537$ kg m², $I_{yy} = 0.3536$ kg m², and $I_{zz} = 0.2918$ kg m². Both the center of gravity and moments of inertia are calculated from SolidWorks (CAD). Three pulleys are employed to connect the buoy to the PTO: two at the wave basin and one at the gantry. The line that connects the buoy to PTO is 3 mm Dyneema rope, made of polymer fibers with high stiffness in tension.

2.1.3. Measurements

The position of the translator is measured by a draw-wire position sensor with a measurement range of 1000 mm, a resolution of 0.3 mm, and a maximum wire acceleration of 5 g (5×9.81 m/s²), where wire retraction (minimum) and wire extension (maximum) forces are 1 N and 1.6 N, respectively. The buoy motion in six degrees of freedom is tracked by a Qualisys system (Qualisys, 2021) using four cameras with a sampling rate of 300 Hz. The force data is collected by two load cells: one connected to the bottom of the buoy and the other to the translator at the gantry. In this paper, the results are presented for the load cell connected to the PTO translator. Each load cell has a capacity of 2000 N, accuracy of $\pm 0.3\%$ of the rated capacity, and a mass of 150 g excluding its cable, with different sealing IP classes of 68 and 65 for the wet and dry environments, respectively. The data is logged and transmitted by two seven-gram SG-Link-200-OEM which communicate with 50 μ s node synchronization through radio frequency (RF) with one LORD Sensing WSDA gateway. Eight wave

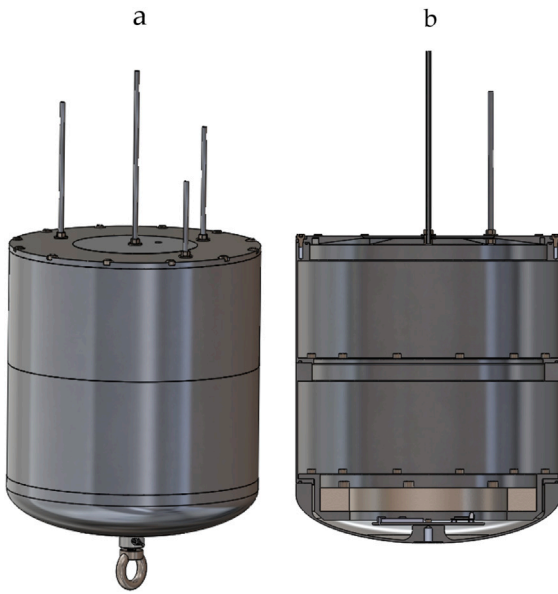


Fig. 3. Buoy with the scale 1:30 where a, and b show the 3-d view and section view, respectively, retrieved from Shahroozi et al. (2021).

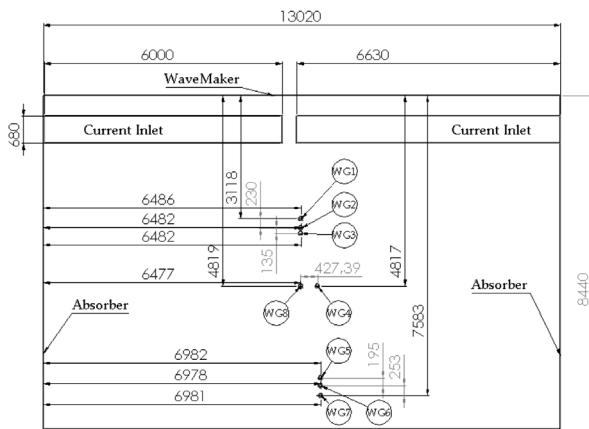


Fig. 4. Wave tank dimensions (in millimeter) and wave gauges positions where the buoy is situated in the location of wave gauge 8.

gauges are used to measure the surface elevation: three in front of the buoy, three at the back, and two at close vicinity to the buoy with the same distance from the wavemaker. The buoy is located at 4.819 m from the wavemaker and 6.477 m and 6.54 m from the side walls. Fig. 4 shows the arrangement of the wave gauges during the wave calibration in the empty wave tank, i.e. without the PTO and buoy. After the wave calibration, the buoy is positioned at the location of WG8. Given the wave tank dimensions, an optimum position for the buoy is chosen considering both wave development and avoiding the effect of wall reflections on the buoy's dynamic. The wavemaker consists of 30 snake type wave paddles which are controlled individually by electric motors (Aalborg-University, 2020). The water depth is 0.73 ± 0.02 m.

2.1.4. Experimental setup uncertainties

Computing the PTO friction damping force of 7.4 N and 18.9 N involves two times derivation of the displacement to achieve the acceleration in order to derive the friction force. Thereby, the introduced noise level due to derivation, and low pass filtering applied to the data result in some degree of uncertainty. The same filtering uncertainties

Table 1
Experimental system properties.

Description	Value	Unit
PTO		
Mass	2.138 ± 0.001	kg
Stroke length	220	mm
End-stop spring coefficient	5.9	N/mm
End-stop spring uncompressed length	60	mm
End-stop spring compressed length	28	mm
Buoy		
Mass	15.73 ± 0.001	kg
Diameter	330	mm
Height	380	mm
Draft	230	mm
Center of gravity (x_{CG}, y_{CG}, z_{CG})	$0 \times 0 \times 118.6$	mm
Moment of inertia (I_{xx}, I_{yy}, I_{zz})	$0.3537 \times 0.3536 \times 0.2918$	kg m ²
Wave tank		
Dimension ^a	$13 \times 8 \times 1.5$	m
Buoy's position from wavemaker	4.819	m
Buoy's position from side walls	6.477, 6.54	m
Water depth	0.73 ± 0.02	m
Sensors		
Position sensor measurement range	1000 ± 0.3	mm
Load cell capacity	2000	N
Qualisys ^b	4 cameras	-
Wave gauges ^c	8 probes	-

^aDimension of active test area: length \times width \times depth.

^bQualisys has a sampling rate of 300 Hz.

^cWave gauges and data acquisition have a sampling rate of 256 Hz.

can be identified for the line force data that is collected by the load cell. Although the essence of uncertainties is clear, the precise quantification of them is not straightforward due to their dependency on both filtering characteristics and measurement errors.

Note that the Qualisys system has some missing data points which may or may not be due to the water overtopping. Usually, when the data is lost for milliseconds, it is due to the Qualisys camera deficiency while in other times, it is due to the overtopping phenomenon.

The summary of the experimental setup properties is given in Table 1. More information on the design of the experiment can be found in Shahroozi et al. (2021).

2.2. Sea states and waves

The sea states are chosen for the waves with a 50-year return period from environmental contour using the I-FORM Hybrid method for the Dowsing site located at 56 km from the west coast of the United Kingdom in the North Sea. More information about the environmental contour method can be found in Wrang et al. (2021) and Katsidoniotaki et al. (2021).

2.2.1. Irregular waves

Irregular waves are generated based on the JONSWAP spectrum (Veritas, 2010) as:

$$S_J(\omega) = A_\gamma S_{PM}(\omega) \gamma \exp\left(-0.5\left(\frac{\omega - \omega_p}{\sigma \omega_p}\right)^2\right) \quad (1)$$

where γ is a non-dimensional peak shape parameter that is considered here as 3.3. The spectral width parameter, σ , is $\sigma_a = 0.07$ for $\omega \leq \omega_p$, and $\sigma_b = 0.09$ for $\omega > \omega_p$. Also, $A_\gamma = 1 - 0.287 \ln(\gamma)$ is a normalizing factor, and S_{PM} is the Pierson–Moskowitz (PM) spectrum defined as:

$$S_{PM}(\omega) = \frac{5}{16} H_s^2 \omega_p^4 \omega^5 \exp\left(-\frac{5}{4} \frac{\omega}{\omega_p}\right) \quad (2)$$

where H_s and ω_p are the significant wave height and the peak angular frequency, respectively. The analytical and experimental spectral density of the surface elevation are shown in Fig. 5. The significant wave

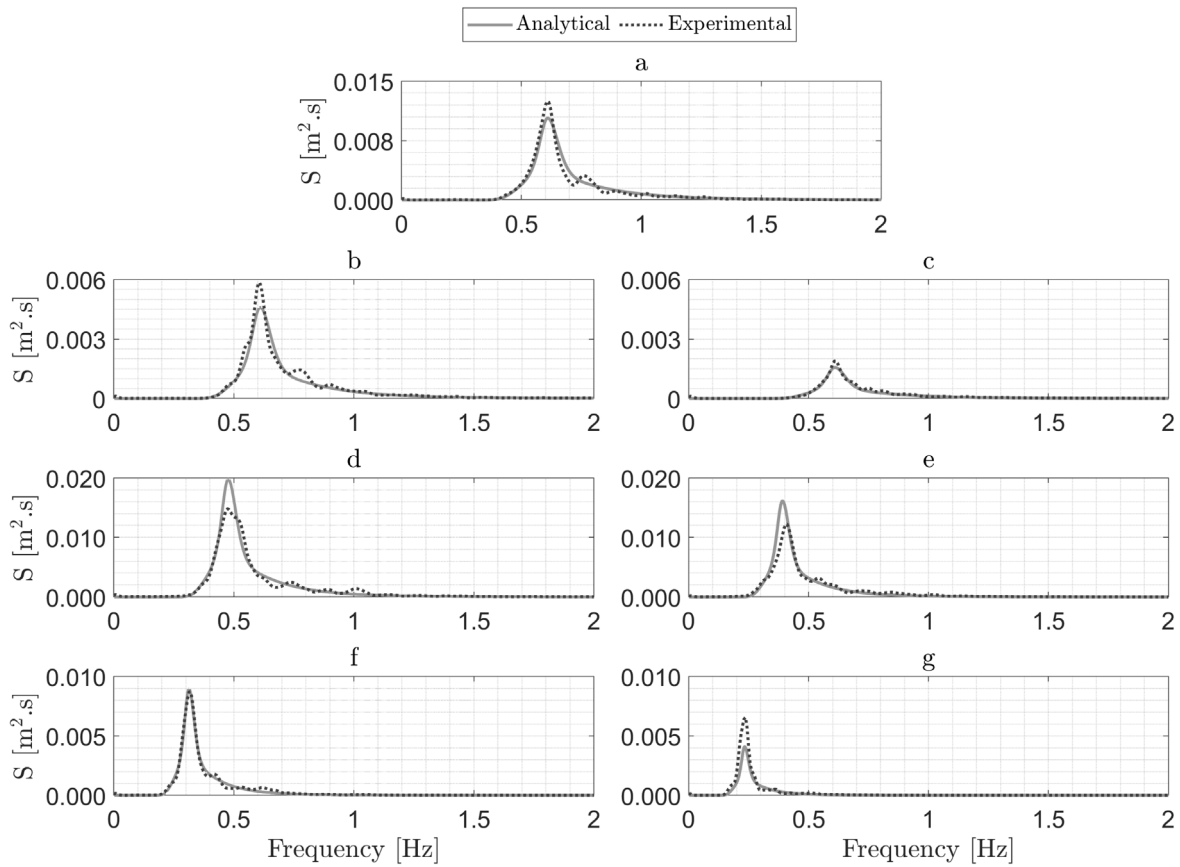


Fig. 5. Comparison of the experimental and analytical spectral density of the surface elevation in the generation of irregular waves where a, b, c, d, e, f, and g demonstrate sea states 5a, 5b, 5c, 6, 8, 9, and 10, respectively. The waves are measured at wave gauge 8 during an empty wave tank (the buoy and PTO are not installed).

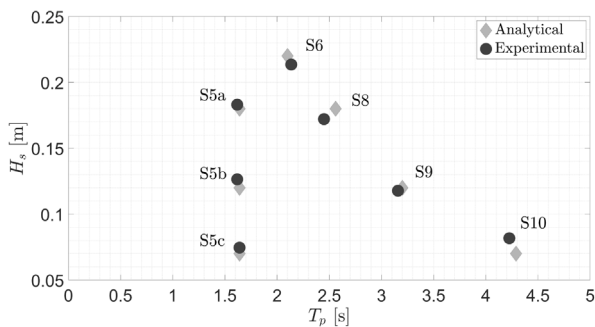


Fig. 6. Comparison of H_s and T_p for the experimental and analytical data in irregular waves. The waves are measured at wave gauge 8 during an empty wave tank (the buoy and PTO are not installed).

height, H_s , and peak period, T_p are computed based on the JONSWAP spectrum for the experimental data, see Fig. 6.

2.2.2. Regular waves

The equivalent regular waves are computed based on irregular waves with wave period $T = T_z$ where T_z is the average zero up-crossing period and wave height $H = 1.9H_s$ in which the value 1.9 is derived from the assumption that the wave height follows the Rayleigh distribution during extreme wave conditions (Veritas, 2010; Yu et al., 2015; Katsidoniotaki et al., 2020). Fig. 7 illustrates the regular waves calibration where the discrepancy seen at the trough between the analytical and experimental data can be explained by the steepness

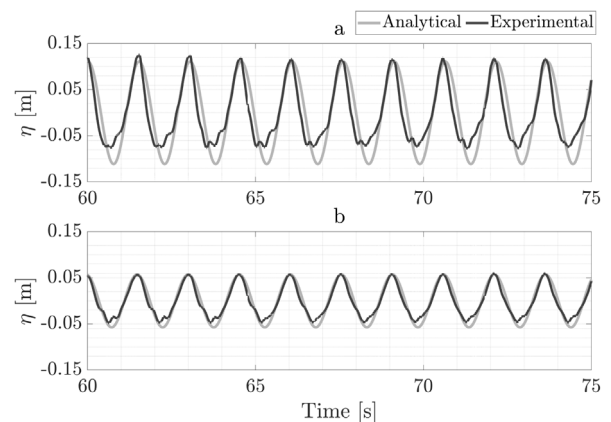


Fig. 7. Comparison of the experimental and analytical regular waves where a, and b present sea states 9 and 10, respectively. The waves are measured at wave gauge 8 during an empty wave tank (the buoy and PTO are not installed).

of the waves, the dimension of the wave tank, and the influence of the intermediate water depth, h , that is considered here. Intermediate waves, $1/20 < h/L_p < 1/2$ where L_p is the wavelength based on the peak period, are affected by the wave tank bed, and thereby, the wave celerity depends on both water depth and wavelength (Chakrabarti, 1987).

2.2.3. Focused waves

A focused wave is composed of superposing large number of harmonic waves at a single position and time. In this experiment, focused waves are defined based on Gaussian wave packet (Claus and Bergmann, 1986), however, other methods such as NewWave theory are also common for generating focused waves (Tromans et al., 1991; Hann et al., 2015; Katsidoniotaki et al., 2020, 2021). Both above-mentioned methods are well defined and representative and the choice of one against the other is highly dependent on the focused wave generation method in the wave tank lab facility as it is the case here.

The Gaussian wave packet may be introduced as (Claus and Bergmann, 1986):

$$\eta_G(x, t) = \int_{-\infty}^{\infty} S_G(k) \exp(i(kx - \omega t)) dk \quad (3)$$

where k is the wavenumber, x and t are the focused position and time, respectively, and $S_G(k)$ is the Gaussian-shaped amplitude spectrum defined as:

$$S_G(k) = \frac{A_0}{\epsilon\sqrt{2\pi}} \exp[-(k - k_0)^2/2\epsilon^2] \quad (4)$$

where A_0 is the amplitude crest, and ϵ is the standard deviation of the Gaussian amplitude spectrum which may also be nominated as its bandwidth or form factor. By defining the dispersion relation, $\omega(k) = gk \tanh(kh)$, and using Taylor expansion, Eq. (3) can be rewritten as real and imaginary parts:

$$\begin{aligned} \eta_G(x, t) &= A_0^4 \sqrt{\frac{1}{1 + \epsilon^4 N^2 t^2}} \\ &\exp\left[-\frac{1}{2} \frac{\epsilon^2}{1 + \epsilon^4 N^2 t^2} (x - Mt)^2\right] (\cos P + i \sin P), \quad (5) \\ P &= k_0 x - \omega_0 t + \frac{\operatorname{atan}(-\epsilon^2 N t)}{2} + \frac{\epsilon^4 N t}{2} \frac{1}{1 + \epsilon^4 N^2 t^2} (x - Mt)^2 \end{aligned}$$

where M and N are interpreted as group velocity and damping factor, respectively, and can be derived as:

$$\begin{aligned} M &= \left. \frac{d\omega}{dk} \right|_{k=k_0} = \frac{C_0}{2} \left[1 + \frac{2k_0 h}{\sinh(2k_0 h)} \right] \\ N &= \left. \frac{d^2\omega}{dk^2} \right|_{k=k_0} = C_0 h \left[\frac{1 - 2k_0 h \coth(2k_0 h)}{\sinh(2k_0 h)} - \right. \\ &\quad \left. \frac{1}{2 \sinh(2k_0 h)} \left(\frac{\sinh(2k_0 h)}{2k_0 h} - \frac{2k_0 h}{\sinh(2k_0 h)} \right) \right] \quad (6) \end{aligned}$$

with $C_0 = \sqrt{\frac{g}{k_0} \tanh(k_0 h)}$.

The Gaussian wave packet, Eq. (5), can be defined by three terms: damping term referring to the first part of the equation, modulation function, i.e. the exponential part, and oscillation term, i.e. the sinusoidal part of the equation. Here, the amplitude crest, $A_0 = \sqrt{2m_0 \ln(n)}$, is defined based on the largest amplitude expected in a 3-hour sea state in $n=1000$ waves (Hann et al., 2015; Katsidoniotaki et al., 2020, 2021), in which m_0 is the zeroth spectral moment. Focused waves are generated based on amplitude crest, peak period, and standard deviation of the Gaussian amplitude spectrum, see Table 2, as input to the wavemaker software. The focused wave calibration is shown in Fig. 8.

Note that the chosen waves are rather steep, and thereby, the generated waves may never replicate the theoretical ones that are based on linear theory.

2.3. Wave types steepness

While the wave steepness of regular waves is a well-known parameter (H/L) that can be used to differentiate linear from non-linear waves (Pecher and Kofoed, 2017), for irregular waves, the definition of wave steepness is more complex and of a stochastic nature.

There are several studies that tried to describe the irregular wave's steepness. For instance in Toffoli et al. (2010), an explanation was

provided for the maximum steepness by studying the irregular waves recorded from open sea as individual waves through zero down-crossing, which gives the definition of steepness at the wave front, and zero up-crossing, which provides the steepness definition for the wave rear. The steepness for each individual wave was defined as the wavenumber times half of the wave height, i.e. the lowest and highest vertical distance in wave elevation in one individual wave. They also studied the statistical properties of extreme waves in a wave tank for a couple of random waves for spectral conditions with steepness $k_p H_s/2 \leq 0.16$ and $k_p H_s/2 > 0.2$ where k_p is the wavenumber associated with the peak frequency. More studies on the steepness of irregular waves can be found in Rue (1993), Tayfun (2006) and Askar et al. (1995).

Here, we use $k_p H_s/2$ merely as an indicative parameter for the steepness of irregular waves as Toffoli et al. (2010) to compare the steepness of sea states relative to each other.

Lastly, the focused wave's steepness is specified as $k_p A_0$ so as (Ning et al., 2009; Hann et al., 2015; Katsidoniotaki et al., 2021) where A_0 is the crest amplitude and k_p is the wavenumber as aforementioned.

2.3.1. Waves' generation uncertainties

The Qualisys system has a lag of 20 ms from wave gauges. Also, it should be noted that the surface elevation data provided here corresponds to the buoy location at equilibrium position and as the buoy is displaced in heave and surge, it no longer corresponds to the exact wave that is impacting the buoy. For both irregular and regular waves, the first 50 s of the data is disregarded to allow the full development of the waves in the wave tank.

Table 2 shows the theoretical sea state information.

3. Extreme waves' phenomena

3.1. Wave breaking

In non-breaking waves where the linear potential theory is applied, the water particles trajectory can be described as circles, and ellipsoids with constant horizontal semi-axis for deep and shallow water, respectively. Thereby, the water particles at the wave crest move at a slower speed than the phase velocity. When the water particles' velocity at the crest exceeds a limiting value, which is defined by the most energetic waves with the same wavelength and water depth, wave breaking will occur (Cokelet, 1977). The wave breaking proceeds with non-linear and turbulent kinetic energy and induces large loads on marine structures. The breaking waves may be classified into four types: spilling, plunging, collapsing, and surging (Veritas, 2010). Having a zero slope in this experiment, the breaking waves fall in the spilling type category. Each breaking wave type can be distinguished by a non-dimensional parameter, $\beta = \frac{H_b}{gT^2 m}$ where m is the beach slope and H_b is the wave height at breaking, and T is the period. Usually, breaking occurs for $\beta > 5$ in spilling breakers, for $0.1 < \beta < 5$ in plunging breakers, for $\beta < 0.1$ in surging breakers, and for $\beta \approx 0.1$ in a collapsing type that is a transition type between plunging and surging breakers (Veritas, 2010).

Identifying whether the waves in a particular sea state break may be pursued using breaking criteria (Liu et al., 2011; Miche, 1944; McCowan, 1894; Munk, 1949; Goda, 2010). Goda (2010) presented a formula for the breaking index for a range of mild and zero beach slope, using the following equation:

$$\frac{H_b}{h} = \frac{B}{h/L_0} (1 - \exp[-1.5\pi \frac{h_b}{L_0} (1 + 11s^{4/3})]) \quad (7)$$

where H_b is the breaking wave height, h is the water depth, and s is the beach slope. Also, B is the proportionality coefficient of breaking index which for irregular waves is between 0.11 and 0.13, for regular waves is 0.17, and for focused waves is between 0.12 and 0.18. Further, L_0 is the deep water wavelength of small amplitude waves that is computed based on: $L_0 = (g/2\pi)T^2$. Note that according to Goda,

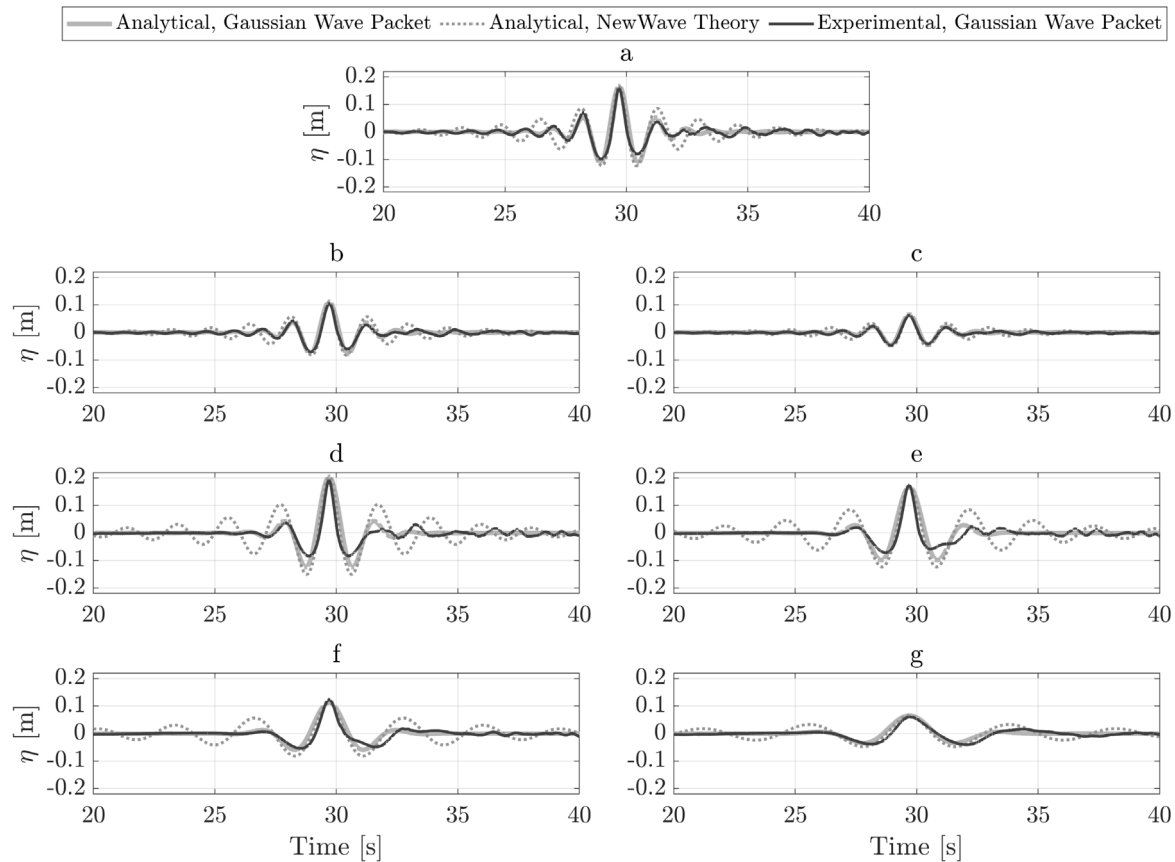


Fig. 8. Comparison of the experimental and analytical focused waves based on Gaussian and NewWave theory, where a, b, c, d, e, f, and g demonstrate sea states 5a, 5b, 5c, 6, 8, 9, and 10, respectively. The waves are measured at wave gauge 8 during an empty wave tank (the buoy and PTO are not installed).

Table 2
Sea state information.

Sea state	H_s [m]	T_p [s]	$k_p H_s / 2$ [-]	A_0 [m]	$k_p A_0$ [-]	ϵ [1/m]	H [m]	T [s]	H/L [-]
S5a	0.18	1.64	0.1572	0.1700	0.2969	0.720	-	-	-
S5b	0.12	1.64	0.1048	0.1150	0.2009	0.700	-	-	-
S5c	0.07	1.64	0.0611	0.0682	0.1191	0.700	-	-	-
S6	0.22	2.10	0.1382	0.1700	0.2135	0.530	-	-	-
S8	0.18	2.56	0.0891	0.1500	0.1485	0.400	-	-	-
S9	0.12	3.20	0.0461	0.1150	0.0885	0.327	0.2223	1.52	0.0691
S10	0.07	4.29	0.0196	0.0682	0.0383	0.230	0.1143	1.52	0.0356

Miche limit (Miche, 1944) of $H_0/(L_f)_0 = 0.142$ is only valid for deep water wavelength of the finite-amplitude waves, i.e. $(L_f)_0$. Goda also mentioned that according to the findings of Yamada and Shiotani (1968) at the breaking limit of the permanent waves, the wavelength is 119.3% of small wave amplitude wavelength. Thus, the multiplication of 119.3% with the Miche breaking limit of 0.142 gives the breaking limit for regular waves which Goda further modified to 0.17.

Using experimental data and Goda criteria for zero beach slope ($s = 0$), Fig. 9 presents the proximity of each sea state to the breaking index line where L_0 is computed based on T_p for irregular and focused waves. Fig. 9 shows that sea states 5a and 6 are more susceptible to breaking for both focused and irregular waves. Comparing Fig. 9 with the experimental observation, neither of the sea states in focused waves show signs of clear breaking before or at the buoy position whereas in irregular waves, clear breaking is detected for some of the waves in sea states 5a and 6 which are mainly before the buoy position. Minimal breaking is noticed at the very crest for a few waves of sea state 8 (irregular waves) both close to the wavemaker and far from the buoy during the experiment.

3.2. Overtopping

Overtopping is another non-linear phenomenon that is a function of the wave height and wave period (Kofoed, 2002). It mainly occurs when a large wave height exceeds the top surface of the buoy which is identified by R_c that is the vertical distance from the steady-state water level to the top of the structure and is called crest freeboard in ship applications, Salauddin and Pearson (2020). The overtopping phenomenon is usually reported in terms of average discharge whose time variation is rather difficult to quantify in the laboratory environment. In this work, the clear indication of overtopping is only qualitatively discussed by tracking two points on the top surface of the buoy, that is the top right and left corners of the buoy's cross-section with the body-fixed $x-z$ plane, see Fig. 10. Qualisys provides the buoy's motion data for the center of gravity which are transformed for point A and B following:

$$z_A = z_{CG} + r \sin(\theta + \phi) \tag{8}$$

$$z_B = z_{CG} + r \sin(\theta - \phi)$$

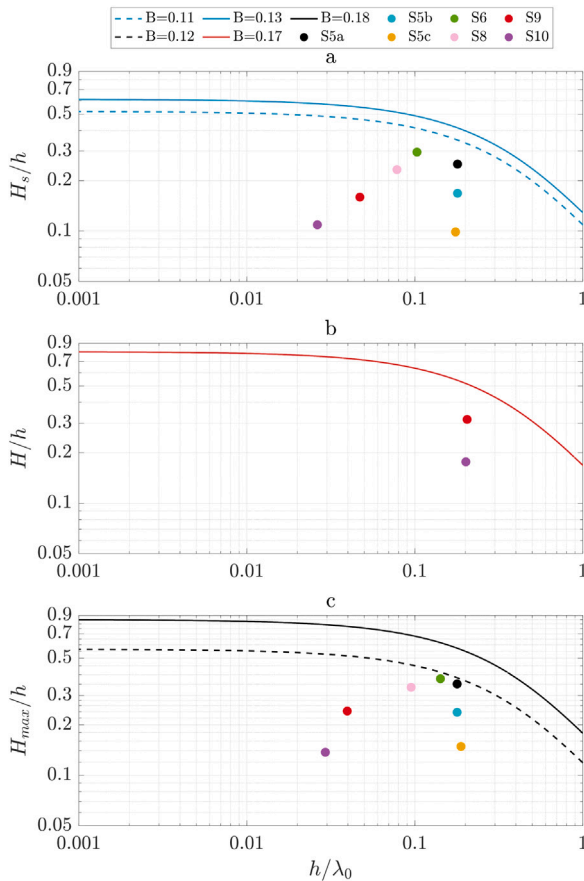


Fig. 9. Evaluation of wave breaking considering Goda criteria where a, b, and c represent irregular, regular, and focused waves breaking in respect to breaker index.

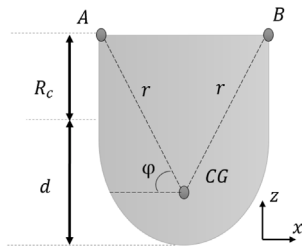


Fig. 10. Buoy's schematic for computing clear overtopping where d is the draft and R_c is the vertical distance from the water level to the top of the buoy.

where z_A and z_B are the heave trajectory of point A and B, z_{CG} is the heave position of the center of gravity, θ is the pitch angle, r is the distance from the center of gravity to point A and B, and angle ϕ is as indicated in Fig. 10.

3.3. Slamming

Slamming (water impact) loads are due to sudden high water pressure acting on the buoy within a short time duration (ms). The complexity of the slamming phenomenon lies in its strong non-linear nature that is sensitive to relative motion and deadrise angle of the body with respect to the free water surface level, its random process that is difficult to be predicted with statistical methods, its short duration of impact which leads to high hydro-elastic effects, and its compressible and partially supersonic flow due to air trapping where water and air

interact (Molland, 2011). The conditions that contribute to slamming are high relative velocity between body and water, the rise of the device above the water surface, and shallow draught.

The effect of slamming force is usually studied as a 2-d (two-dimensional) phenomenon following von Karman theory (Von Karman, 1929), who studied the water impact on a landing airplane based on momentum conservation and simplifying the slamming effect by neglecting the surface elevation and by assuming a small deadrise angle. Wagner (1932), further proposed a more realistic formula that gives a conservative peak impact pressure by compensating for the pile-up effect however still by assuming a small deadrise angle and excluding the effect of air trapping.

Linear slamming theories usually consider infinite cylinders or bodies of rotational symmetry and approximate the fluid as inviscid, irrotational, incompressible, and free of surface tension. Moreover, the effect of gravity is assumed negligible (Molland, 2011). Although today's 2-d theories try to capture this phenomenon as close to reality as possible by combining theories with empirical corrections, the slamming is yet a strong non-linear phenomenon that should be analyzed in three dimensions for which there exists few studies, however, more improvement may still be required for these models to become advantages over simplified 2-d models.

For a point-absorbing device, the slamming may be studied for two main categories: bottom slamming (De Backer et al., 2010, 2008, 2009), which is due to the water impact with the buoy when dropping after being lifted above the water surface which results in a sudden change in the vertical acceleration of the buoy; and wave breaking slamming, which is due to the horizontal impact of the bulk of water with a high relative velocity at the wave crest with the buoy.

The horizontal (surge) force acting on a floating slender body due to wave breaking impact has the main contribution from inertia, drag, and slamming. For more accurate quantification of the wave impact for non-slender bodies, whose diameter is not negligible in comparison to the wavelength such as the one here, the wave radiation damping and diffraction forces need also to be taken into account, Sawaragi (1995). Slamming and drag have quadratic relation with a relative velocity between the wave crest and the body, and inertia is proportional to the relative acceleration between buoy and fluid particles (Veritas, 2010). Hence, the contribution of each force may be summarized as (Veritas, 2010):

- The drag contribution is fairly steady when breaking waves pass the buoy;
- The inertia is proportional to the relative horizontal acceleration and the submerged volume of the buoy;
- Slamming is quite short in time and drops to zero after its impact.

The sum of the inertia and drag, that are quasi-static and horizontal forces, is expressed as Morison equation (Wienke et al., 2001):

$$F = \rho V_s \dot{u} + \rho C_d V_s (\dot{u} - \dot{x}_b) + \frac{1}{2} \rho C_d A_d (u - \dot{x}_b) |u - \dot{x}_b| \quad (9)$$

where V_s is the submerged volume of the body, A_d is the characteristic drag area, ρ is the water density, C_d and C_a are the drag and added mass coefficients, respectively, u is the flow velocity, and \dot{x}_b is the body surge velocity. The last term in the equation is the drag force, and the first and the second terms constitute the inertia force and are referred to as the Froude-Krylov force and hydrodynamic mass force, respectively. In Wienke et al. (2001), the slamming impact force F_s on a fixed rigid slender cylinder was derived by introducing curling factor, λ , that is dependent on wave breaking type, and by being inspired from von Karman theory. Hence, $F_s = \rho R u^2 C_s \lambda \eta_b$ where the drag coefficient over time, t , is $C_s = \pi(1-tu/R)$, $\lambda \eta_b$ is the height of the impact area, and R is the radius of the cylinder. Note that for a floating body, the relative velocity, $u - \dot{x}_b$, instead of water celerity, u , should be used. In Wienke et al. (2001), it was noted that the impact force derived from Wagner theory yields more realistic values due to consideration of the pile-up effect.

In this experiment, the buoy is not subjected to the bottom slamming, and only wave breaking slamming is observed. This study covers the qualitative analysis of water breaking slamming and no pressure sensor is deployed on the buoy.

4. Results

4.1. Effect of different wave types

One important objective of this study is to understand the dynamics and extreme forces in different wave-type representations (irregular, regular, and focused waves) of the same sea state.

Fig. 11 shows a large discrepancy between irregular and focused waves for sea states 6, 8, and 10 for most of the damping cases. Irregular waves in these sea states give rise to higher peak line force compared to focused waves. Note that the maximum line force data points that are missing for some sea states and damping configurations in Fig. 11 are not tested during the wave tank experiment due to time constraints. Before further inspection of Fig. 11, it is worth reviewing the generation of Gaussian focused waves. The bandwidth parameter (ϵ) defines the number of wave components that are superposed in a Gaussian wave packet, see Eq. (3). Within the same sea state, a larger bandwidth means quicker dispersion of Gaussian wave packet with one major peak at the focused position and time and notably smaller side peaks in the time domain. Now looking back to Fig. 8 and Table 2, sea states 5a, 5b, and 5c have the largest bandwidth parameter with considerably larger side peaks in comparison with other sea states. This implies the importance of the selection of the bandwidth parameter that should be considered individually for each sea state.

It is common to study extreme waves for focused waves generated based on NewWave theory as (Rafiee and Fiévez, 2015; Hann et al., 2015; Ransley et al., 2017; van Rij et al., 2019). Seeing that the bandwidth parameter has a significant effect on the shape of the focused waves which can directly influence the magnitude of the peak force, the Gaussian focused waves are further analytically compared to the equivalent focused wave using NewWave theory, as it is presented in Fig. 8. Gaussian focused waves in sea states 5a, 5b, 5c, and 10 replicate more the shape of the NewWave focused waves, while for other sea states, a larger deviation is observed. In sea states 5a, 5b, and 5c, the focused waves give similar maximum force to the irregular waves, see Fig. 11, while this is not the case for sea state 10. On the other hand, the peak forces obtained in sea state 9 for focused and irregular waves are similar while the generated focused wave deviates significantly from the analytical one from the NewWave theory. Hence, it is important to mention that it is not straightforward to translate the irregular waves to focused waves of the same sea state. Therefore, the comparison of one sea state to another in focused waves should be considered with care. More information about the comparison of different wave types can be seen in Appendix A.

4.2. Effect of significant wave height and peak period

The peak forces for all sea states for focused and irregular waves are illustrated in Fig. 12 where results are also compared for all four PTO damping configurations of D_0 , D_1 , D_2 , and D_∞ .

For irregular waves, as it is shown in Fig. 12a, sea state 6, with the largest H_s , gives rise to the highest peak force among all sea states. In the comparison of sea states with different peak periods (T_p), higher H_s does not necessarily associate with a higher peak force. Let us take sea states 9 and 10 as an example. In damping cases, D_1 and D_2 , the peak force in sea state 10 is similar to the one in sea state 9 while sea state 10 has a smaller significant wave height but a larger wavelength or peak period. Hence, waves that have lower H_s but longer T_p , may rise high peak forces compared to the waves with higher H_s and shorter T_p . Although sea states 8 and 5a have the same significant wave height, sea state 8 with a larger wave peak period does not show higher peak

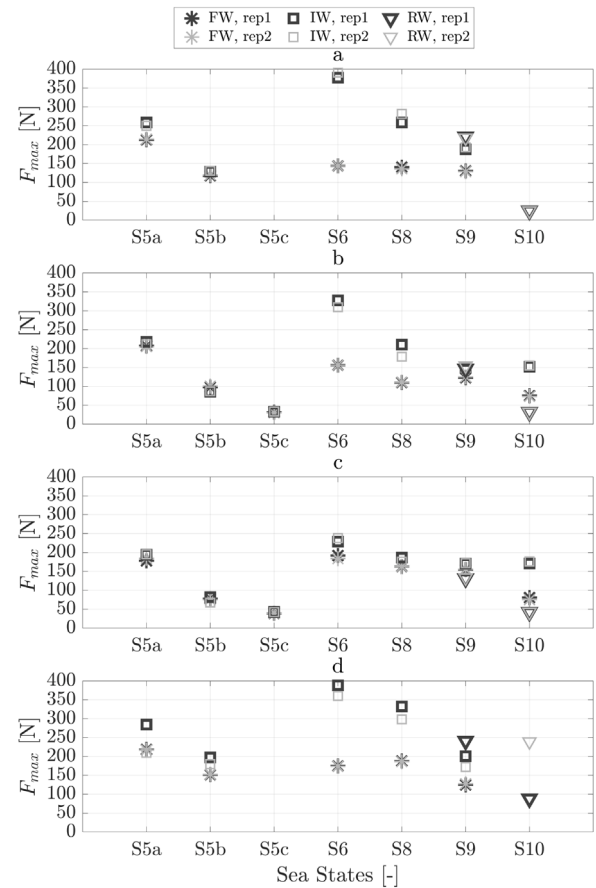


Fig. 11. Maximum line force for all sea states where a is for D_0 ; b for D_1 ; c for D_2 ; and d for D_∞ .

line force, see Fig. 12a, in contrary to the comparison of sea states 5b and 5c with sea states 9 and 10, respectively. It is important to note that in sea state 8 for irregular waves, shown in Fig. 12a for damping case D_1 , the load cell data for repetition two is missed at the end of the time series for a few seconds during which the peak force in repetition one has occurred, and therefore, the peak forces are deviating in these two repetitions. Also, for damping case D_0 , a maximum force similar to sea state 5a is seen for sea state 8 in the first 22 s of the data. However as previously mentioned, the first 50 s of the data is disregarded to let the sea state fully develop in the wave tank and it is intended to keep the criteria unified for all sea states and wave types. Therefore, in the comparison of sea states 5a and 8 for D_0 , this may be considered. Regardless, significant wave breaking for a few waves in sea state 5a during the experiment has been observed unlike sea state 8, the effect of which on the line force should not be ignored. The effect of wave breaking is narrated in Section 4.5. The D_∞ case in which the PTO translator is locked introduces more constraints and non-linearity in the dynamics of the buoy and thereby hinders the repeatability of the line force results.

Fig. 12b shows a different result pattern in terms of the order of peak line forces between sea states. Sea state 5a appears to give a larger peak force compared to others although as explained in Section 4.1, the reason to lower peak force of the sea state 6 in focused waves may be due to the choice of the bandwidth parameter in the generation of focused waves.

Still looking at Fig. 12b, increasing the significant wave height results in higher peak line force in the sea states with the same peak period, i.e. sea states 5a, 5b, and 5c ($T_p = 1.64$ s), and this effect

can also be seen for irregular waves in Fig. 12a. The effect of H_s is further studied in Fig. 13, where the maximum line force occurs for sea state 5a with the largest significant wave height ($H_s = 0.18$ m) for all damping configurations. In addition, sea state 5c with the smallest significant wave height ($H_s = 0.07$ m) shows the lowest peak force for damping cases of D_1 and D_2 . Sea state 5c is not tested for other damping configurations of D_0 and D_∞ , although the same observation can be expected considering this trend. The sensitivity to T_p is displayed in Fig. 14 that compares sea states 5b ($T_p = 1.64$ s) and 9 ($T_p = 3.2$ s) which have the same significant wave height of 0.12 m in sub-figures a to d, and sea states 5c ($T_p = 1.64$ s) and 10 ($T_p = 4.29$ s) with the same significant wave height of 0.07 m in sub-figures e and f. Sea states with larger peak periods show significantly larger peak forces. Looking to sea state 9 at zero PTO damping configuration, the high number of peaks is associated to the compression of the end-stop spring owing to a larger surge amplitude which has a direct effect on the PTO translator motion. The end-stop effect is explained in detail in Section 4.4.

Surge compared to heave motion has considerably larger amplitude in sea states 9 and 10 in comparison with 5b and 5c, respectively, as shown in Figs. 15, 16, and 17 for focused waves. Hence, the PTO translator is mainly affected by the surge motion, and thereby, it results in higher peak line force in sea states 9 and 10 compared to 5b and 5c, respectively. The same pattern can be seen for irregular waves in Fig. 18 compared to Fig. 19. Looking back to Fig. 14 and sea state 9 for D_0 in focused waves, it can be seen that the maximum line force occurs far after the focusing time, i.e. 29.7 ± 0.05 s. This is also due to the large amplitude of surge motion between 31 and 32 s as a result of a long peak period which leads to full compression of the end-stop spring and consequently maximum line force, see Fig. 16 for damping D_0 for a closer inspection. The same can be said for sea state 8. Moreover, in this time interval, the PTO translator hits the end-stop with a higher velocity which can be seen from the slope of the PTO position curve. Another interesting observation is the heave motion in comparison of sea states 9 and 5b and sea states 10 and 5c in Figs. 15 to 17. The heave motion in sea states 5b and 5c show higher amplitude than 9 and 10, which is related to the effect of the natural frequency of the system as it is discussed in Section 4.8, however, it has a small impact on the peak force due to its smaller motion and velocity amplitude compared to surge motion and velocity.

4.3. Effect of damping

The effect of different damping configurations can be analyzed by investigating the irregular waves as shown in Figs. 18 to 19 and in figures for irregular waves in Appendix B. For sea states 5a and 6, comparing D_0 , D_1 , and D_2 , it illustrates that increasing the damping flattens the peaks of the PTO position (green lines) and hereupon lower peak forces are obtained, as can also be seen in the comparison of peak forces in Fig. 12a. The PTO position is constant throughout at infinite damping coefficient case, i.e. locked PTO. Since the PTO is locked in D_∞ case, the buoy can only have negative heave motion with comparatively smaller fluctuations while the sway amplitude has significantly increased relative to other damping cases where it is almost zero. Again from Fig. 12a, it can be seen that at D_∞ for almost all sea states, the peak forces are elevated as high as zero damping case or even higher. This is the contribution of higher relative velocity between the buoy and water when the buoy is constrained. On the other hand, when the damping is reduced to zero, the WEC experiences higher inertia due to higher accelerations which also produces high peak forces in the event of end-stop spring compression.

It can be concluded that increasing the PTO damping from the zero case, decreases the magnitude of the peak forces, however, we cannot derive a linear relation for this effect. Evidence shows there exists a damping value for which the minimum peak force is obtained. In other words, looking at Fig. 12a, increasing the damping from zero reduces the peak force, but the trend is reversed in high damping values. In

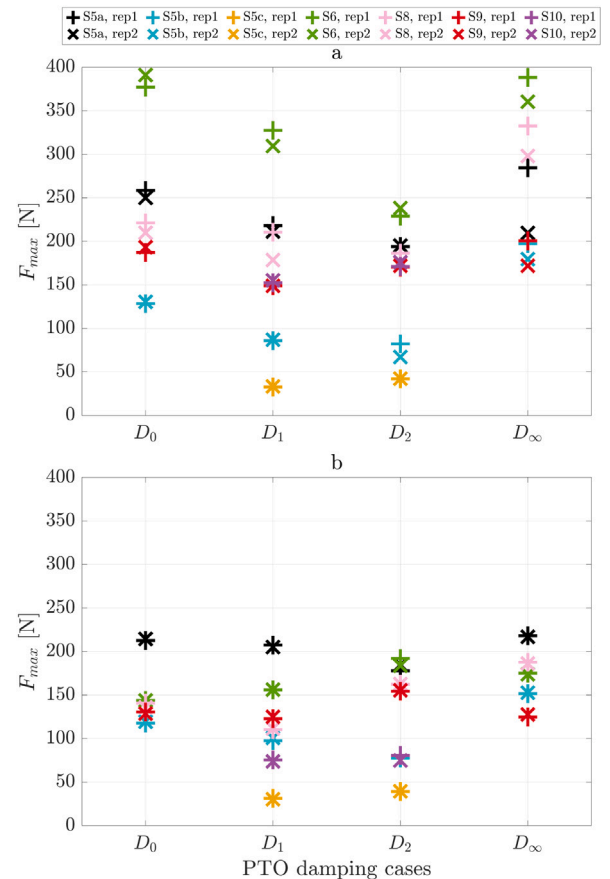


Fig. 12. Maximum line force versus four PTO damping configurations for sea states 5 to 10 where a and b show irregular and focused waves, respectively.

this regime, the peak force reaches its maximum at infinite damping coefficient. For instance for sea state 6, the trough of F_{max} across all damping cases can be found near D_2 and the same conclusion can be drawn for instance for sea state 5a, whereas the trough for sea state 10 appears around D_1 . The D_0 and D_∞ cases provide higher line force compared to other damping configurations. Note that the zero PTO damping case does not correspond to absolute zero damping in the system and the effect of internal friction forces in the pulleys should be considered during the quantitative analysis. The same trend as irregular waves where minimum line force is obtained around D_1 or D_2 can be seen for focused waves in Fig. 12b except for sea state 6. When the damping increases, the heave motion peaks later in time, and in the case of sea state 6, this is closer to both surge motion and surge velocity peaks. This high surge velocity combined with a high surge amplitude results in higher line force which can be seen in Figs. 20 and 21. Thereby, it is the combination of heave and surge amplitude as well as their velocities that defines the peak line force in all sea states.

At D_∞ case for focused waves, sea state 6 achieves lower peak force than D_2 , unlike other sea states. This may be understood through the increasing effect of overtopping which leads to the reduction of the peak force at infinite damping coefficient case. The effect of overtopping is discussed more in Section 4.6.

Another interesting observation is that the surge amplitude is insensitive to damping, unlike the heave amplitude which reduces with higher damping. The reason for the insensitivity of surge amplitude to different damping cases is due to the fact that the waves always push the buoy in surge while depending on the damping, buoy motion may lag or lead (e.g due to springing effect) in time which influences the

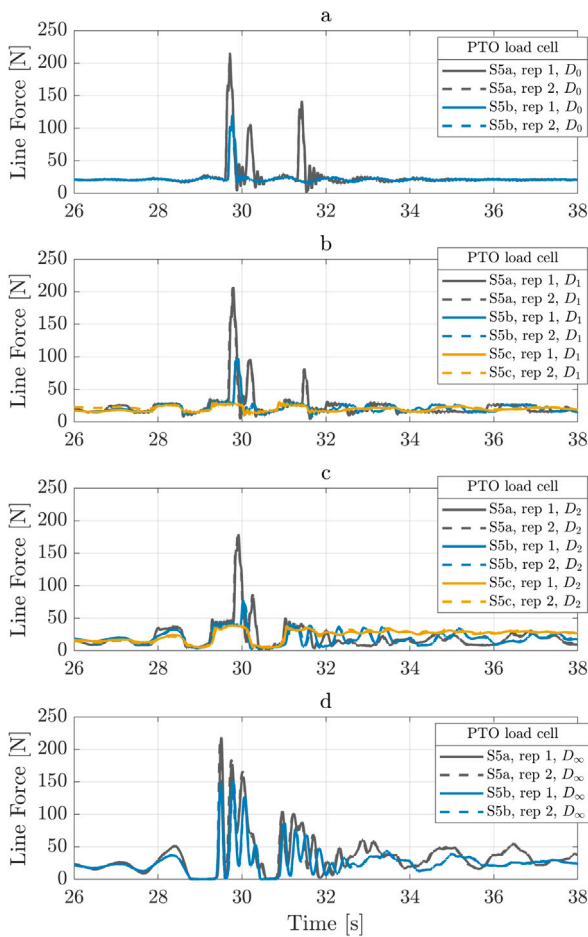


Fig. 13. Comparison of the line force for the focused waves with the same peak period but different significant wave heights. Sub-figures a, b, c, and d show the line force for damping cases of D_0 , D_1 , D_2 , and D_∞ , respectively.

heave motion. Consequently, when the high damping case delays the heave peak, it also reduces the heave amplitude, and depending on the surge position and velocity at this instant, the end-stop can engage more or less. A detailed explanation of the end-stop effect is given in Section 4.4.

4.4. Effect of end-stop

During normal operation, the movement of the PTO translator does not involve compression of the end-stop spring unlike in extreme waves where the end-stop compression is highly likely and its effect on both buoy dynamics and line force is of great importance.

Fig. 22 shows the end-stop effect for irregular waves and for damping cases D_0 , D_1 , and D_2 . The highest number of engagement is seen for zero PTO damping configuration for all sea states and increasing the damping decreases the number of end-stop spring compression significantly in both repetitions, see Fig. 22 and sub-figures a and d. Sea state 6 with the highest significant wave height ($H_s = 0.22$ m) displays the highest number of engagements among all sea states. The intensity of the end-stop spring compression is introduced by computing the root-mean-square (RMS) of the spring length after being compressed. Sea state 5a depicts the highest RMS of the end-stop spring compression in both repetitions, see Fig. 22 and sub-figures b and e. Moreover, it can be seen that the number of the end-stop engagement does not directly correlate to the intensity of the end-stop spring compression, e.g. sea state 5a in D_2 has a higher intensity compared to D_0 . A direct relation

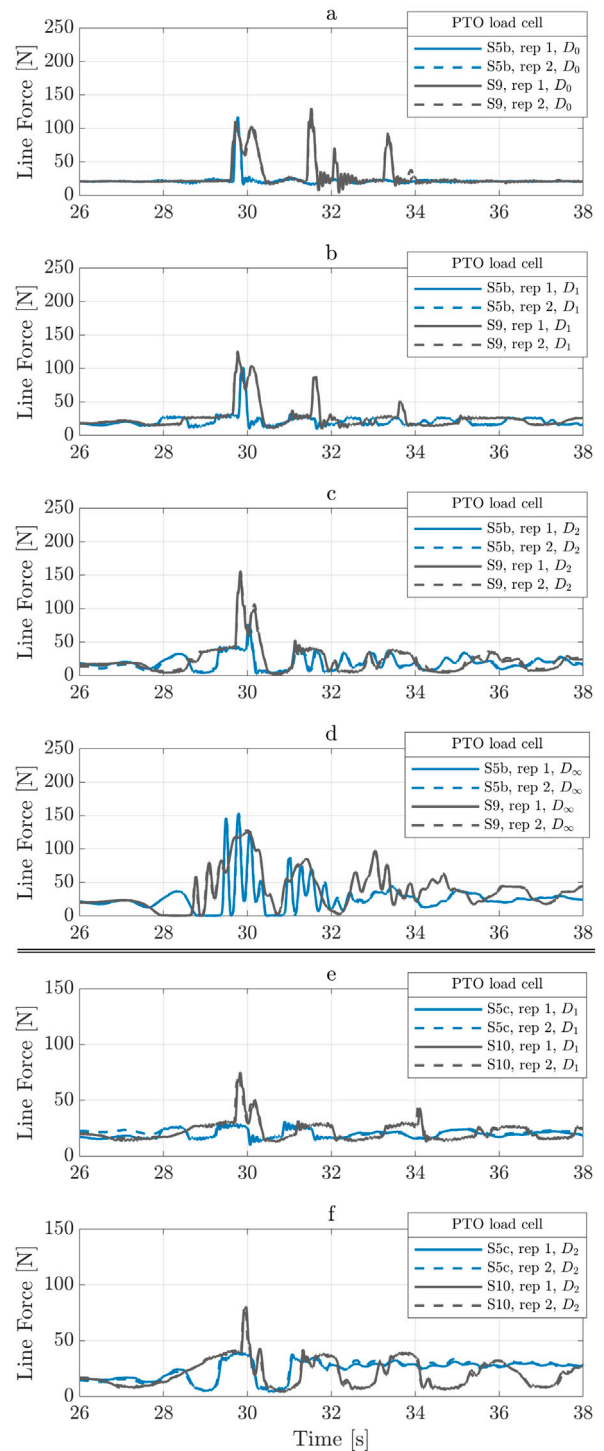


Fig. 14. Comparison of the line force for the focused waves with the same significant wave height but different peak periods. Sub-figures a, b, c, and d show the line force for sea states 5b and 9 for damping cases of D_0 , D_1 , D_2 , and D_∞ , respectively. Sub-figures e and f show the line force for sea states 5c and 10 for damping cases of D_1 , and D_2 , respectively.

can be seen for root-mean-square of forces after compression of the end-stop spring to the number of engagements, see Fig. 22 and sub-figures c and f. Note in Fig. 22, the root-mean-square of the line forces instead of the peak forces as presented in previous figures is studied. Sea states 5c

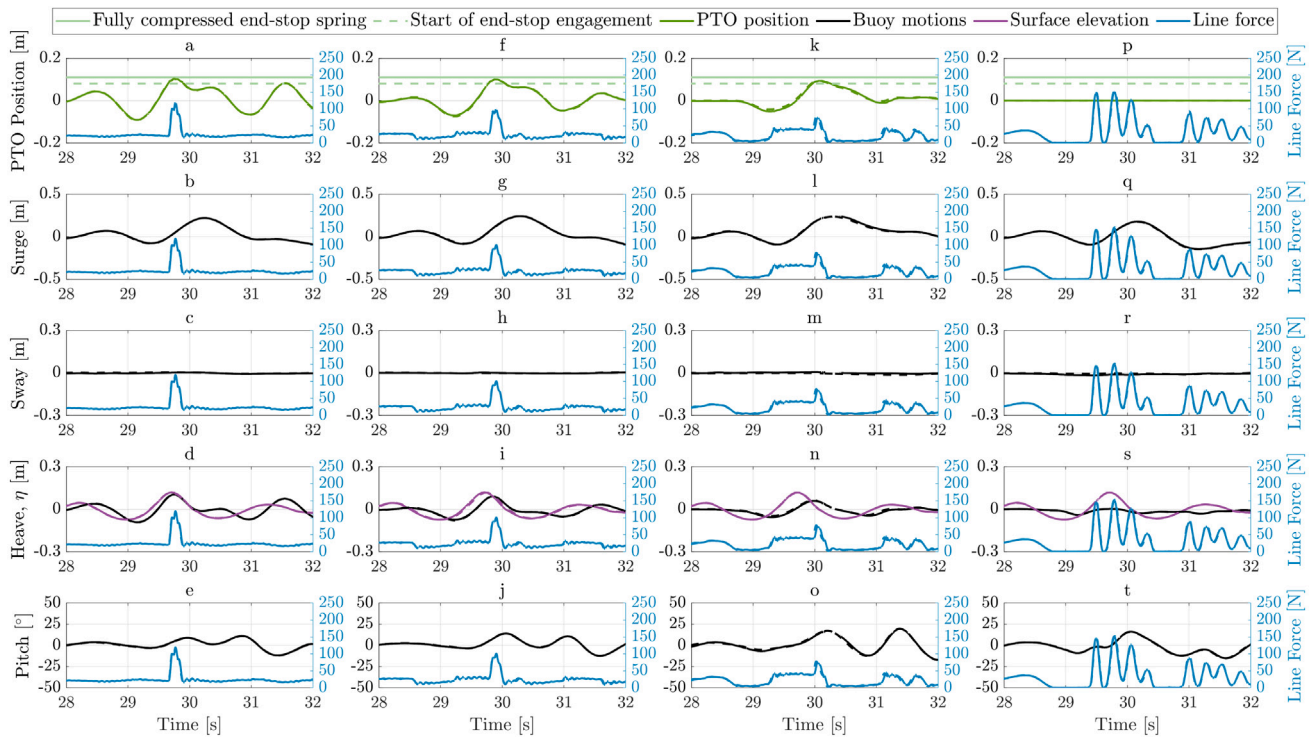


Fig. 15. Buoy's motions and line force in focused waves for sea state 5b where $a, b, c, d,$ and e represent damping D_0 ; $f, g, h, i,$ and j represent D_1 ; $k, l, m, n,$ and o represent D_2 ; $p, q, r, s,$ and t represent D_∞ . The surface elevation is η . The solid and dash lines represent the two repetitions except for the end-stop spring lines.

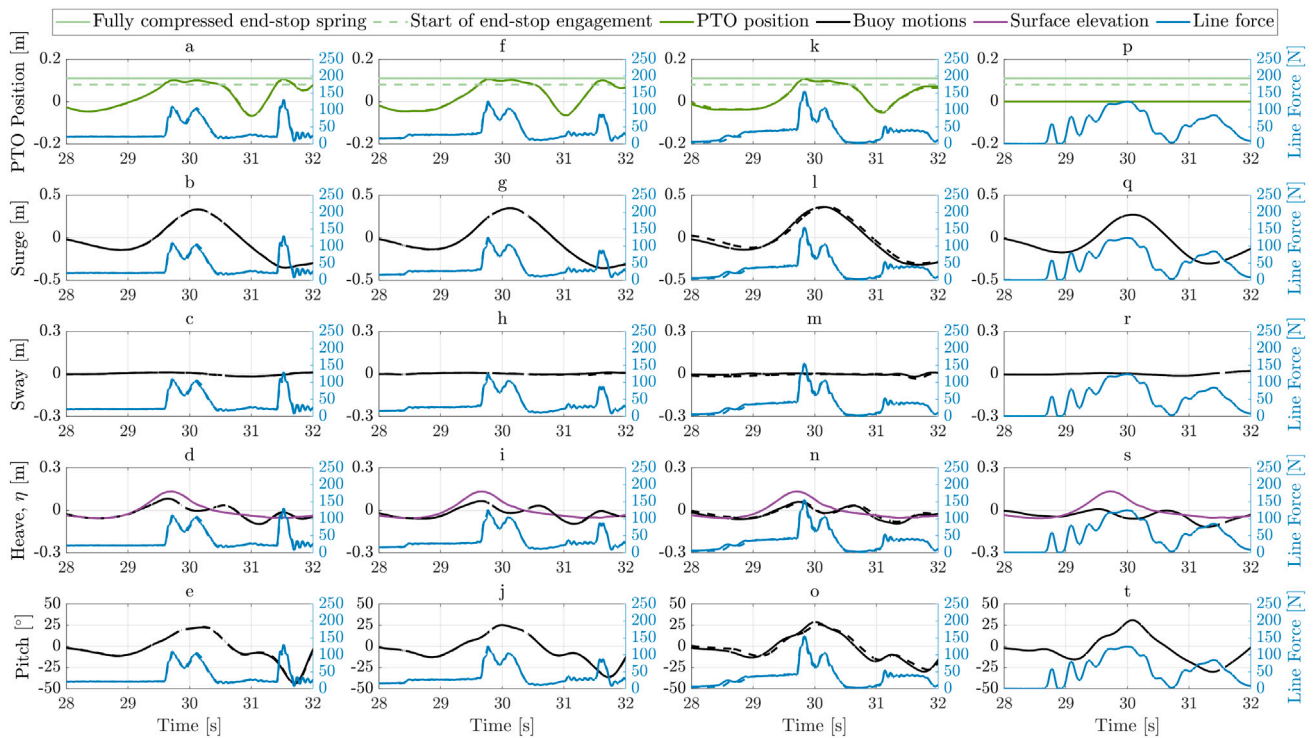


Fig. 16. Buoy's motions and line force in focused waves for sea state 9 where $a, b, c, d,$ and e represent damping D_0 ; $f, g, h, i,$ and j represent D_1 ; $k, l, m, n,$ and o represent D_2 ; $p, q, r, s,$ and t represent D_∞ . The surface elevation is η . The solid and dash lines represent the two repetitions except for the end-stop spring lines.

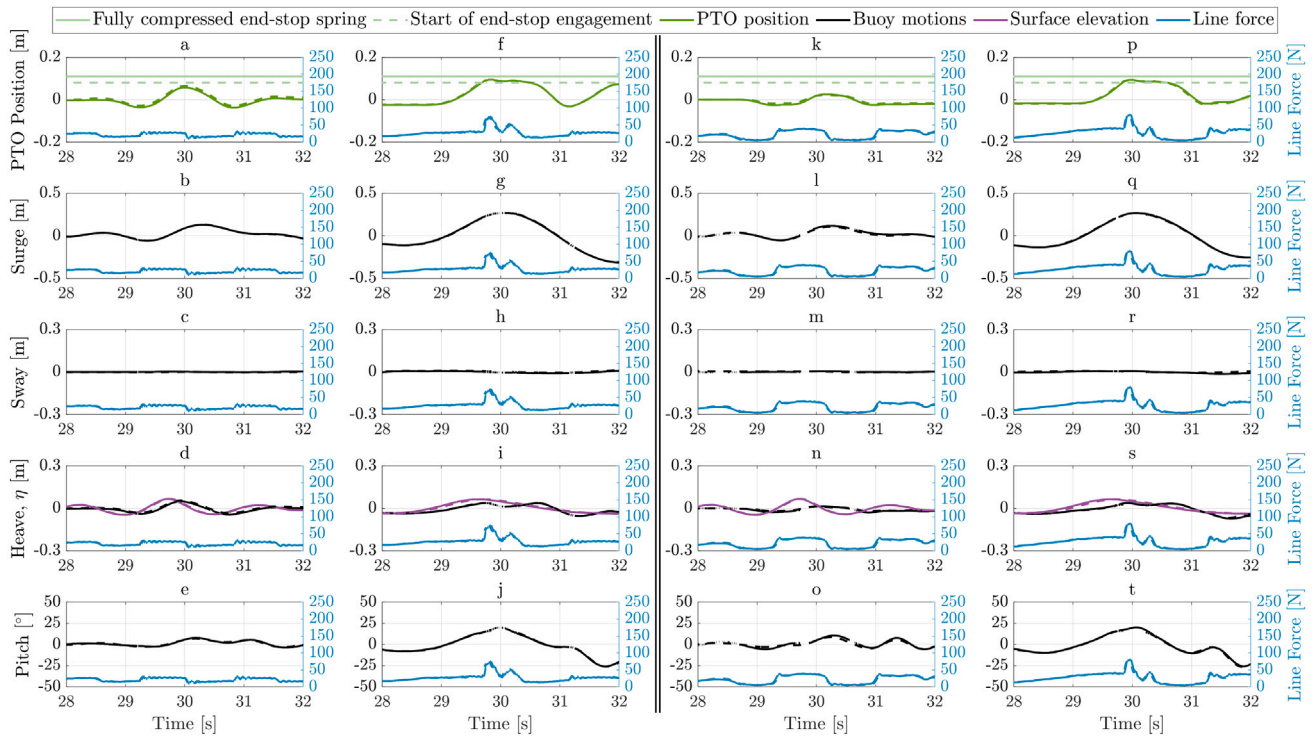


Fig. 17. Buoy's motions and line force in focused waves for sea state 5c and 10 where *a, b, c, d, and e* represent damping D_1 in sea state 5c; *f, g, h, i, and j* represent damping D_2 in sea state 5c; *k, l, m, n, and o* represent damping D_1 in sea state 10; *p, q, r, s, and t* represent damping D_2 in sea state 10. The surface elevation is η . The solid and dash lines represent the two repetitions except for the end-stop spring lines.

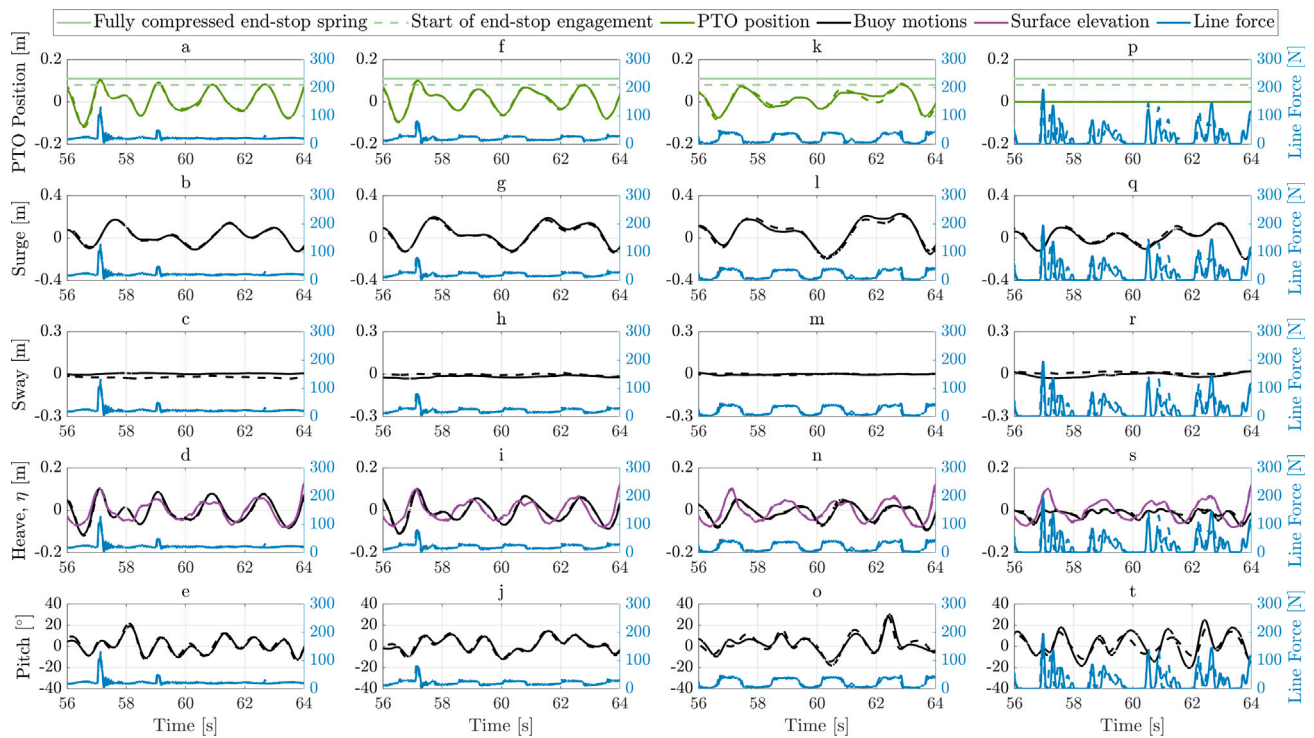


Fig. 18. Buoy's motion and line force in irregular waves for a few seconds in sea state 5b where *a, b, c, d, and e* represent damping D_0 ; *f, g, h, i, and j* represent D_1 ; *k, l, m, n, and o* represent D_2 ; *p, q, r, s, and t* represent D_∞ . The surface elevation is η . The solid and dash lines represent the two repetitions except for the end-stop spring lines. (For interpretation of the references to color in this figure legend, the reader is referred to the web version of this article.)

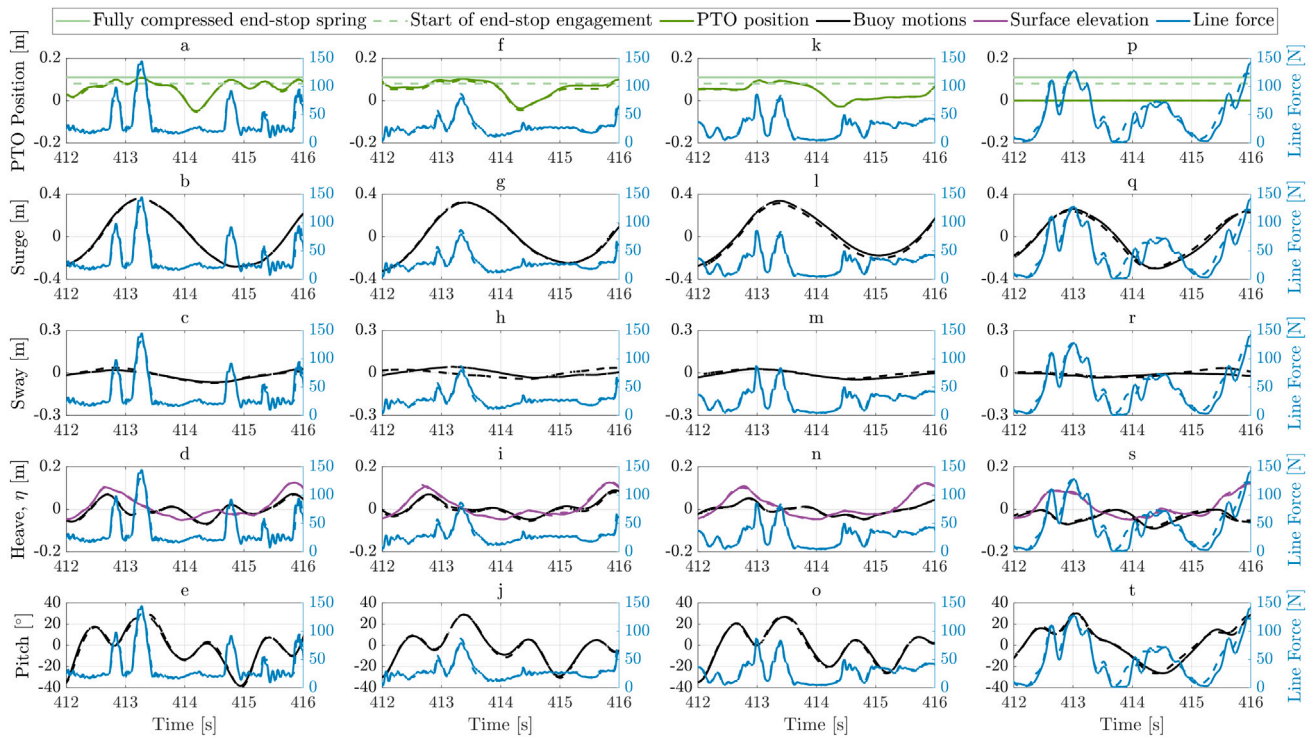


Fig. 19. Buoy's motion and line force in irregular waves for a few seconds in sea state 9 where *a, b, c, d* and *e* represent damping D_0 ; *f, g, h, i*, and *j* represent D_1 ; *k, l, m, n*, and *o* represent D_2 ; *p, q, r, s*, and *t* represent D_∞ . The surface elevation is η . The solid and dash lines represent the two repetitions except for the end-stop spring lines. (For interpretation of the references to color in this figure legend, the reader is referred to the web version of this article.)

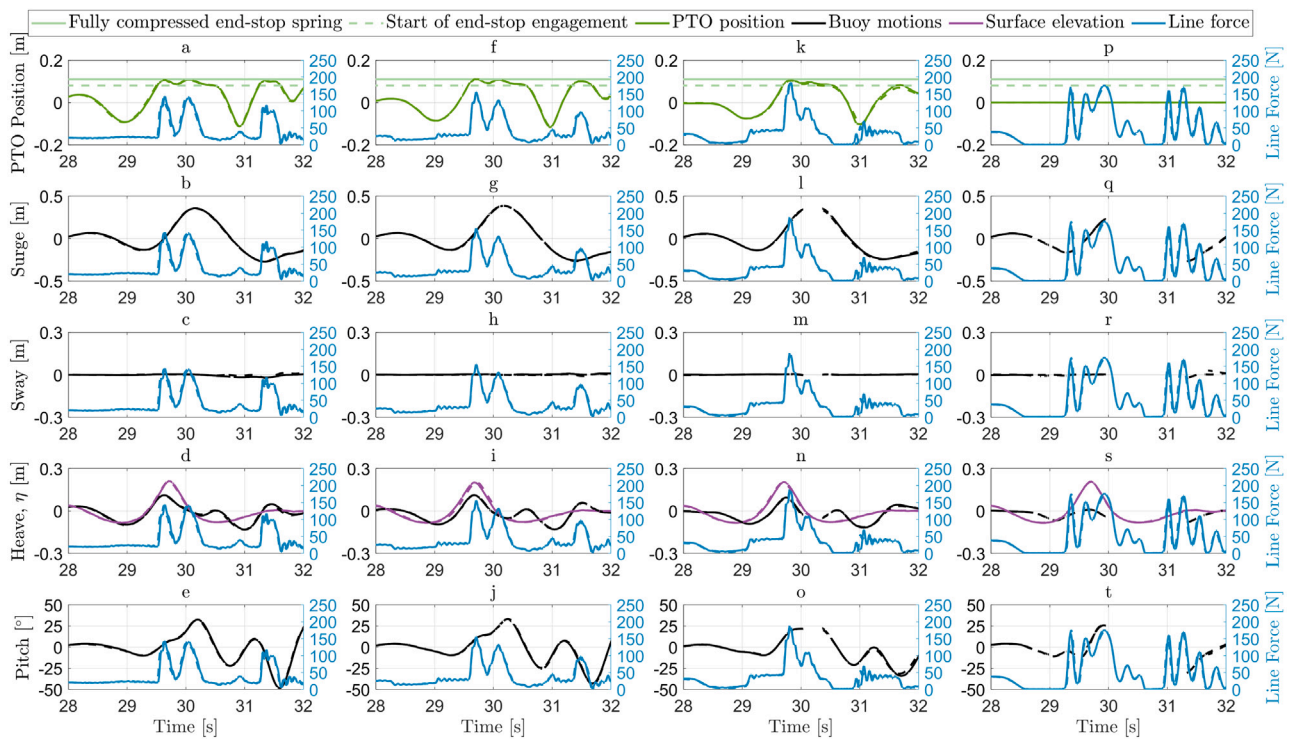


Fig. 20. Buoy's motions and line force in focused waves for sea state 6 where *a, b, c, d*, and *e* represent damping D_0 ; *f, g, h, i*, and *j* represent D_1 ; *k, l, m, n*, and *o* represent D_2 ; *p, q, r, s*, and *t* represent D_∞ . The surface elevation is η . The solid and dash lines represent the two repetitions except for the end-stop spring lines.

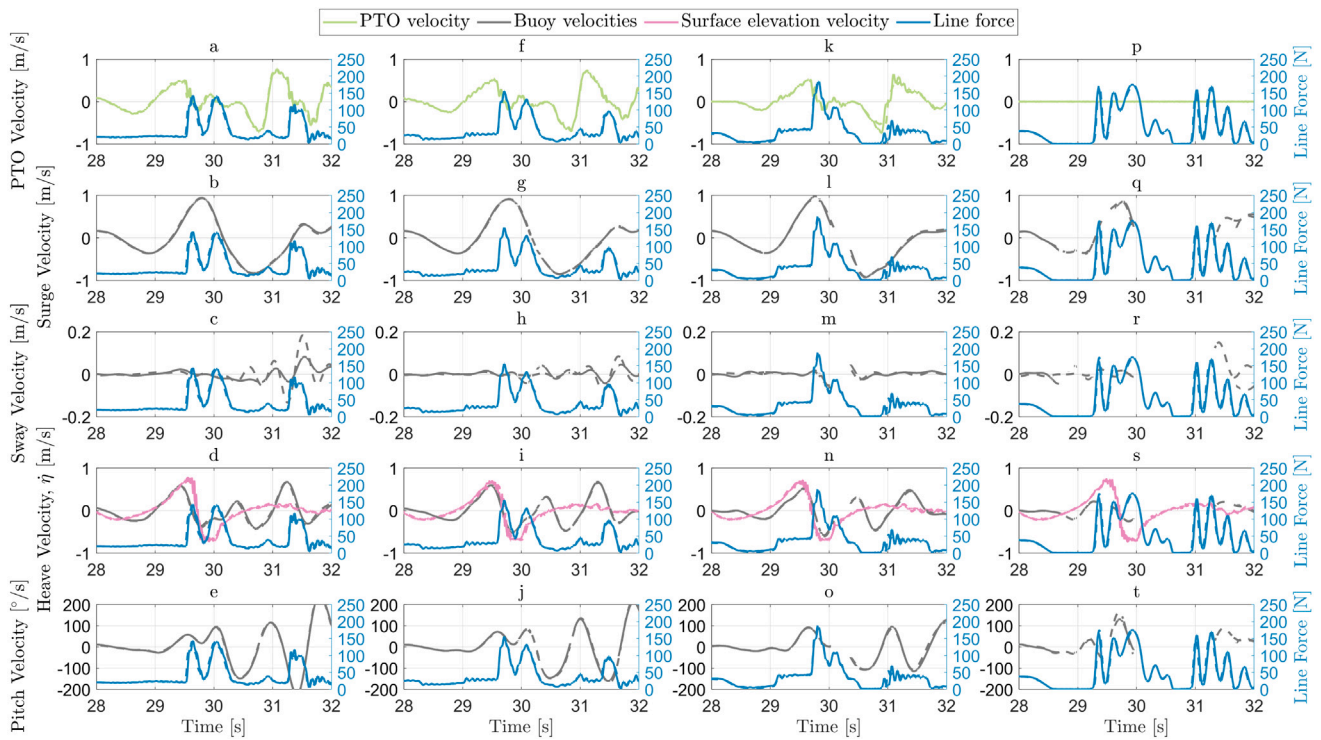


Fig. 21. Buoy's velocities and line force in **focused waves** for sea state 6 where *a, b, c, d, and e* represent damping D_0 ; *f, g, h, i, and j* represent D_1 ; *k, l, m, n, and o* represent D_2 ; *p, q, r, s, and t* represent D_∞ . The surface elevation is η . The solid and dash lines represent the two repetitions except for the end-stop spring lines.

and 10 are not tested for zero PTO damping configuration. Moreover, sea state 5c has no end-stop spring compression in D_1 and D_2 as it is also indicated in Fig. 22.

As the buoy faces less resistive damping from the PTO, the end-stop engages more often, and consequently, a higher force is achieved. Looking from the PTO side, the line force can be obtained from:

$$m_{PTO}\ddot{z}_{PTO} = F_{line} + m_{PTO}g + F_{end-stop} + F_{fPTO} \quad (10)$$

where \ddot{z}_{PTO} and g are PTO's and gravitational acceleration, respectively, m_{PTO} is the mass of the PTO including load cell and other mechanical components connected to the translator such as turnbuckle, F_{fPTO} is the PTO damping force, $F_{end-stop}$ is the end-stop force which is non-zero only when the end stop is engaged.

The dynamics of the line force at the event of the end-stop spring compression together with PTO position is shown in Figs. 15 to 20 and figures in Appendix B in sub-figures *a, f, k, and p*, for both focused and irregular waves. It can be observed that the end-stop spring compression correlates to the sudden peak force which is followed by the line (rope) slacking. Less compression of the end-stop spring for higher damping is seen where the PTO position is also flattened. As the PTO translator is completely locked in D_∞ , there is no end-stop spring compression and the large peak forces are the outcome of higher buoy-water relative velocity that is explained in Section 4.3.

The main reason for the double peak seen in the vicinity of the focused time, e.g. sea state 9 in Fig. 16 for damping D_0 , is the result of the end-stop spring compression, where the first peak is mainly due to the heave amplitude and the second peak occurs mostly owing to a large surge motion.

Lastly, comparing regular waves for sea states 9 and 10, a large difference in peak force is seen in Fig. 11. In addition to a larger wave height for sea state 9, the end-stop has been constantly engaged throughout the operation considering the stroke length of 220 mm, see Appendix A and compare regular waves 9 with 10.

4.5. Effect of steepness and wave breaking

Let us evaluate the effect of steepness and wave breaking for irregular waves and sea states 5a and 8 which have the same significant wave height $H_s = 0.18$ m but different wave periods: $T_p = 1.64$ s for sea state 5a, and $T_p = 2.56$ s for sea state 8. Looking back to Table 2 and Fig. 9, it can be said that sea state 5a has a higher steepness compared to sea state 8, and as a result, clear wave breaking has been observed for this sea state in the experiment. The wave breaking can result in slamming which induces high loads on the device, see Section 3.3. This event is also manifested in Fig. 22, where a larger root-mean-square of the end-stop spring compression is seen in sea state 5a. The kinetic energy of the water particles increases momentarily when the wave is breaking and when these high-velocity water particles hit the buoy, higher surge acceleration is attained which eventually results in compression of the end-stop spring with higher intensity. Following that, sea state 5a has obtained a higher peak line force with its smaller peak period compared to sea state 8. This is not applicable for instance when comparing sea states 9 and 5b or sea states 10 and 5c which also have the same significant wave height, since there is no wave breaking event for either of these sea states.

It may be interesting to also mention that the number of compression of the end-stop spring, for the sea states with the same significant wave height, is associated with a longer wave period, however, this is not the case in terms of root-mean-square of the end-stop spring compression when the waves are breaking, see Fig. 22.

As aforementioned, wave breaking is observed for irregular waves in sea states 5a and 6 during the experiment although it cannot be straight-forwardly seen from Fig. 9. Fig. 23 shows the steepness distribution of the individual waves based on zero up- and down-crossing (see Section 2.3 and Toffoli et al., 2010) at wave gauges 3 and 5 which are installed in the upstream and downstream of the buoy respectively, refer to Fig. 4. Fig. 23 shows a significant reduction in the steepness of the individual waves in wave gauge 5 compared to wave gauge 3 which is another indication of the wave breaking in these two sea states. For

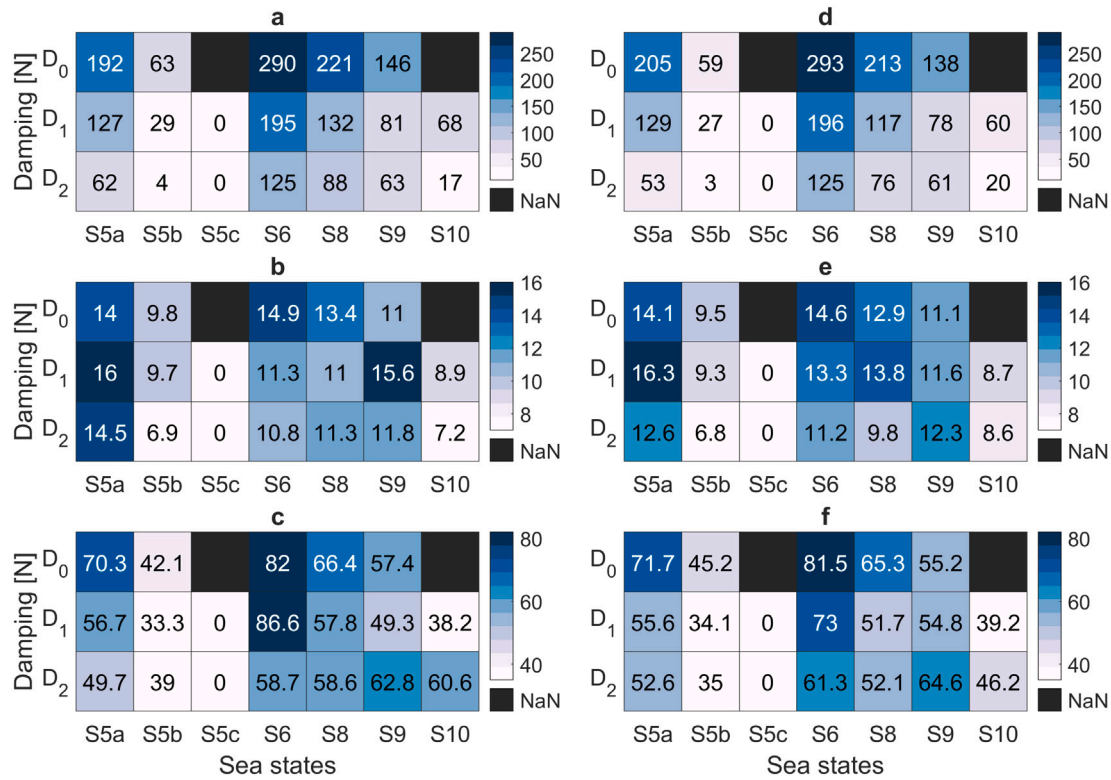


Fig. 22. End-stop effect for irregular waves for three PTO damping of 0, 7.4, and 18.9 N for time intervals of 50 to 600 s where *a* and *d* show the number of end-stop spring compression, *b* and *e* illustrate RMS of end-stop spring compression, and in *c* and *f* RMS of line force after engagement of end-stop spring is shown. The left figure shows repetition one while the right figure shows repetition two.

further comparison, the steepness distribution in the sea state with the lowest steepness (sea state 10) seems to be unchanged.

4.6. Effect of overtopping

The overtopping phenomenon can be seen in Fig. 24 in sub-figures *f* and *g*. In general, increasing the damping constrains the buoy motion in heave, therefore, overtopping in higher damping is more likely to occur.

Here, a clear indication of overtopping is studied by comparing the wave surface elevation with the heave trajectory of points A and B as identified in Section 3.2, see Fig. 25. When overtopping occurs, the water pressure on top of the buoy and the line force act in the same downward direction which eventually reduces the line force magnitude on the buoy. This effect is clearly shown in Fig. 25a for sea state 5a in irregular waves between seconds 191 and 192. At the D_∞ case, the buoy is subjected to even more non-linearities and its analysis is more complex and repetitions do not necessarily replicate one another at all times. Fig. 25b shows overtopping of the wave at the exact same time as Fig. 25a for D_∞ . The missing data for heave trajectories of points A and B, i.e. computed based on Qualisys data, shows that during overtopping the Qualisys markers are completely covered by water. The line force at this event shows a high peak magnitude, however, it is still expected that overtopping has reduced the amplitude of the force.

Note that comparing the heave motion with wave elevation in Figs. 15 to 20 and figures in Appendix B in sub-figures *d*, *i*, *n*, and *s*, to understand the effect of overtopping is irrelevant since the heave motion is reported based on Qualisys data which tracks the center of gravity of the buoy.

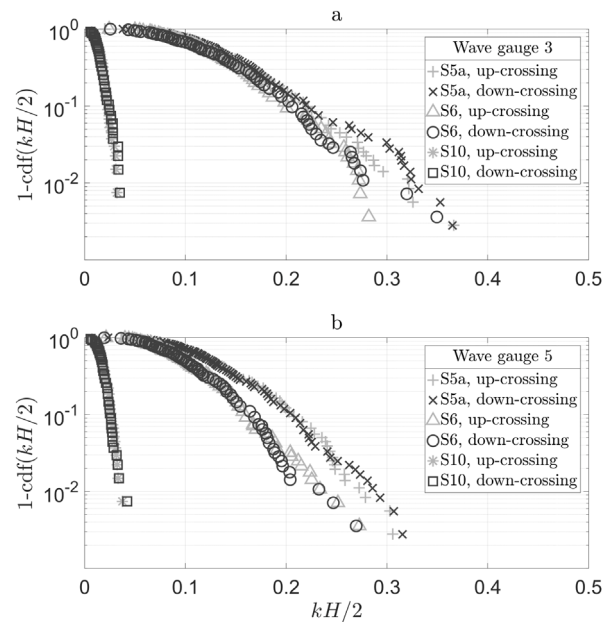


Fig. 23. Steepness distribution for individual zero up-crossing and zero down-crossing waves where *a* shows wave gauge 3 located before the buoy and *b* shows wave gauge 5 located after the buoy.

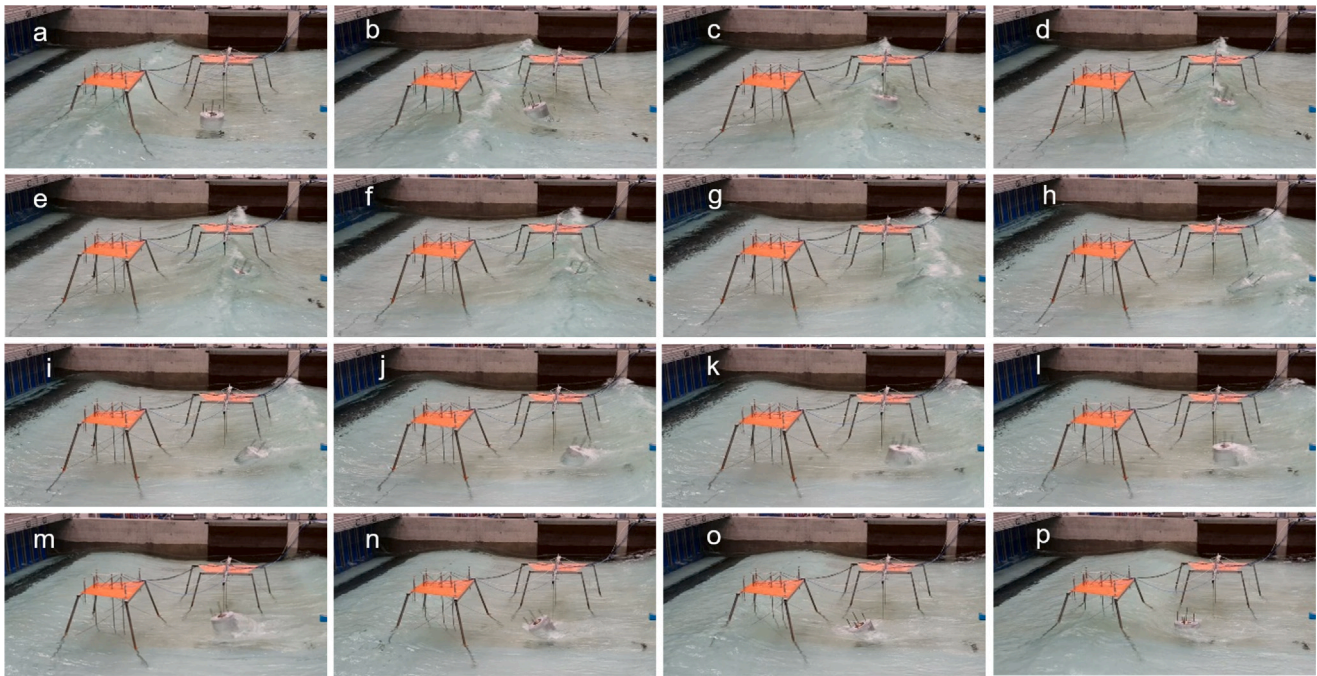


Fig. 24. Buoy's motion during irregular waves in sea state 6 with PTO damping of zero. The alphabet letters show the order in which photos should be seen to capture the sequence of the events and buoy's dynamic.

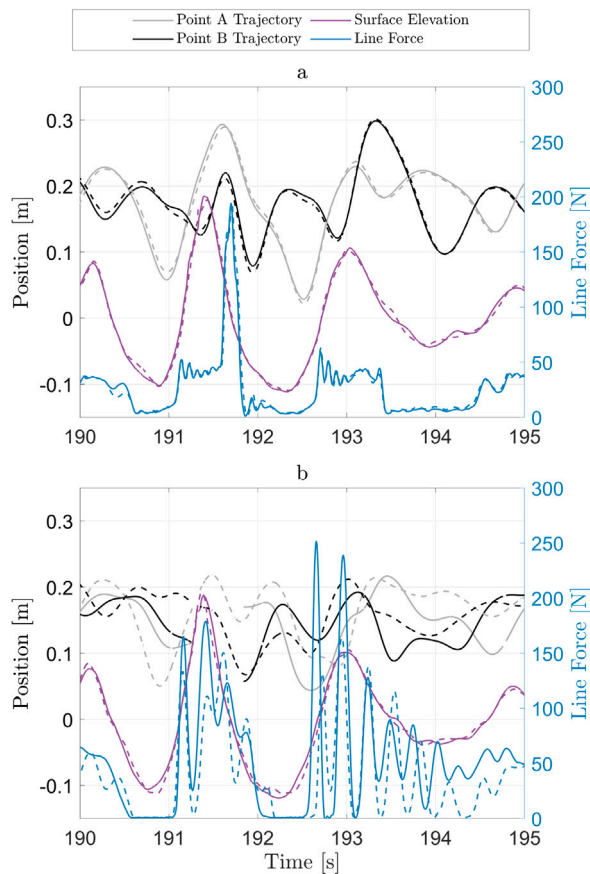


Fig. 25. Effect of clear overtopping in irregular waves for sea state 5a between second 190 and 195, where *a* shows the results for D_2 and *b* for D_∞ . Heave trajectories of point A and B are computed based on Eq. (8).

4.7. Effect of wave breaking slamming

In both irregular and focused waves, peak line forces at D_∞ are clearly elevated higher in comparison with other damping cases, see Fig. 12. This case makes a perfect example for demonstrating the effect of wave breaking slamming since the buoy is constrained in the upward heave motion, although it is free to move downward, and thereby, the influence of the horizontal force due to wave breaking slamming is quite significant.

Through evaluation of the line force dynamics, seen in Appendix A particularly looking at D_∞ , the impact of wave breaking slamming as well as line snap and slack are quite apparent. The snap and slack in the rope lead to frequent fluctuation in the line force which is not present in non-moored floating bodies. Moreover, in other damping configurations, the peak forces are also the result of the end-stop spring compression, see Section 4.4. For sea states 6, and 5a in irregular waves in D_∞ , clear wave breaking is observed during the experiment. The resulting wave breaking slamming leads to a similar line force pattern as line snap and slack which is evidently short in time and drops to zero just after the wave impact.

For a point-absorbing device, the water impact due to wave breaking may be followed by the overtopping phenomenon. In this case, the magnitude of the line force is counteracted by the downward water pressure on the top surface of the buoy which reduces the heave force. Hence, although the horizontal (surge) force increases in the event of wave breaking, the reduced heave component of the total line force may lead to lower peaks.

When the wave breaks and the effect of overtopping is small, the horizontal slamming force gives rise to considerably high peak forces. In Kapsenberg (2018), an interesting study was explained to assess the effect of the wave horizontal force for the waves with and without breaking before hitting a flat plate tilted 15° in the direction of the incoming waves. The flat plate was instrumented with 40 pressure sensors to measure the pressure on different locations of the plate. The results showed a significant difference where not only did the non-breaking waves show lower peak forces but also the force increased in a more gradual trend, unlike the breaking waves. In methodology,

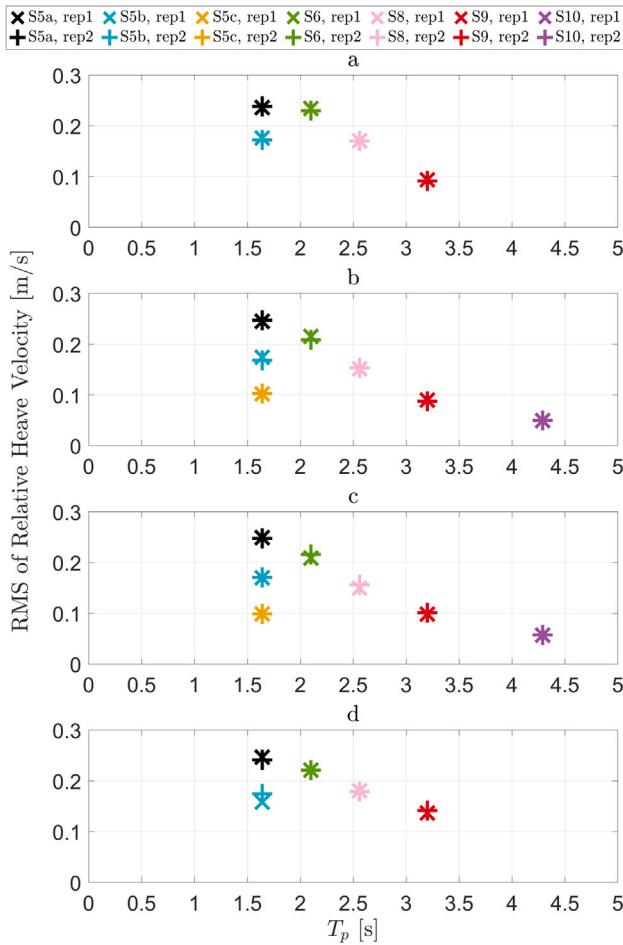


Fig. 26. Comparison of the relative heave velocity for all sea states in irregular waves where a is for D_0 ; b for D_1 ; c for D_2 ; and d for D_∞ .

Section 3.3, we have focused on the horizontal forces so far as they have the main contribution in terms of slamming in this experiment. Now, just touching upon the influence of vertical forces on the system, Fig. 26 shows the root-mean-square of relative heave velocity, that is $\sigma_{v,R} = \sqrt{\Sigma(\dot{z}_b - \dot{\eta})^2}$ versus peak period for all sea states where \dot{z}_b is the velocity of the buoy in heave direction and $\dot{\eta}$ is the surface elevation velocity. Comparing again sea states with the same significant wave height but different peak periods, i.e. sea state 5b with 9 and sea state 5c with 10, shows that sea states 5b and 5c have higher RMS of relative heave velocity. This is explained by the influence of natural frequency in heave, Section 4.8, since sea states 5b and 5c are closer to the natural frequency of the system in heave. Note that sea states 5b and 5c resulted in lower peak forces due to the influence of the horizontal force.

4.8. Effect of natural frequency

Many point-absorber systems are designed to oscillate at their natural frequency to maximize the velocity and thus the power absorption (Falnes and Kurniawan, 2020). Thereby, it is of interest to evaluate the peak line forces from this perspective. In this section, the effect of natural frequency is explained excluding the D_∞ case. The natural frequency (ω_n , that may also be called undamped natural frequency) of the system in heave is derived from decay tests. Assuming a free vibration with viscous damping, this natural frequency is computed as 6.05 rad/s when the PTO is not locked, as explained in Shahroozi et al. (2021). Thus, the wave frequency corresponding to sea states 5a, 5b,

and 5c are considered the closest to the natural frequency of the system in heave.

When looking at Fig. 27, it can be seen that sea states 5a, 5b, and 5c have the highest heave response amplitude operator (RAO). The exception is seen in D_2 for sea state 5c which shows a lower heave RAO compared to other sea states while it should have been otherwise, which is expected to be due to the influence of high friction damping in this sea state with small significant wave height and short peak period which causes a short halt in the motion of the translator.

Now, let us again look into Fig. 12 and compare sea state 5b with 9 and sea state 5c with 10 which have the same significant wave height but sea states 5b and 5c are those with a wave frequency closer to the natural frequency of the system. Interestingly, both sea states 5c and 5b show considerably lower peak line forces. As previously mentioned, the surge motion for sea states 9 and 10 is considerably larger than 5b and 5c. This effect may be seen in Fig. 27 which shows as the peak period increases, the surge RAO also increases. The change in the peak period, while keeping the significant wave height constant, means also changing the wavelength, and therefore, the amplitude of the surge motion is being influenced which has a direct effect on the translator motion. The pitch RAO has the same trend as the surge RAO, see Fig. 27 for pitch.

Regardless of the natural frequency that is discussed in this section, the RAO for D_∞ case (locked PTO) is worth showing, see Fig. 27. Unlike other damping cases, the system in D_∞ configuration is highly influenced by strong non-linearities such as overtopping and frequent line snap and slack, and therefore, the same comparison between the sea states cannot be straightforwardly seen in the surge and pitch RAOs of this damping case. As it is expected, the maximum heave motion becomes negligible which justifies the low (near zero) values in this case.

5. Discussion

Usually, analytically generated sea states are based on the linear theory. Here in this experimental investigation, we show that not only steepness but also intermediate water depth induces non-linear patterns in the waves where troughs are less deep and the peaks are narrower, as indicated in Figs. 6, 7, and 8.

In the comparison of different wave-type representations in this experiment, we find that for the same sea state, changing the wave types does not necessarily give the same peak line force. Careful consideration is required to translate one wave type to another. It should be mentioned that we had some difficulties in selecting the desired bandwidth parameter, ϵ , for generating some of the focused waves based on Gaussian wave packet mainly due to the steepness of the waves and limited capacity of the wave tank. We observe that even for the focused sea states synthesized from Gaussian wave packet, which are fairly replicating the analytical NewWave theory, the maximum line force does not match the one obtained for irregular waves, see sea state 10 in Fig. 11. Comparing the regular and irregular waves is another evidence for the disagreement between the peak force in different wave types within the same sea state, cf. Fig. 11, although only regular waves for two sea states are tested in this experiment. Not to mention that in three of the sea states, i.e. 5a, 5b, and 5c, a similar peak force is achieved in comparison of irregular and focused waves, regardless of the system damping value. It is of interest to experimentally compare the irregular wave's results with peak forces obtained from focused waves based on the NewWave theory. Nonetheless, these experimental results suggest that among different wave types, irregular waves in all configurations show higher peaks for the line force that should be considered as a more conservative choice in the design for survivability of the WECs. The reader should note that the experiment is conducted with regular waves representation for only two of the sea states due to the limited wave tank capability of creating steep waves. Therefore, it is of interest to perform the experiment for the equivalent regular

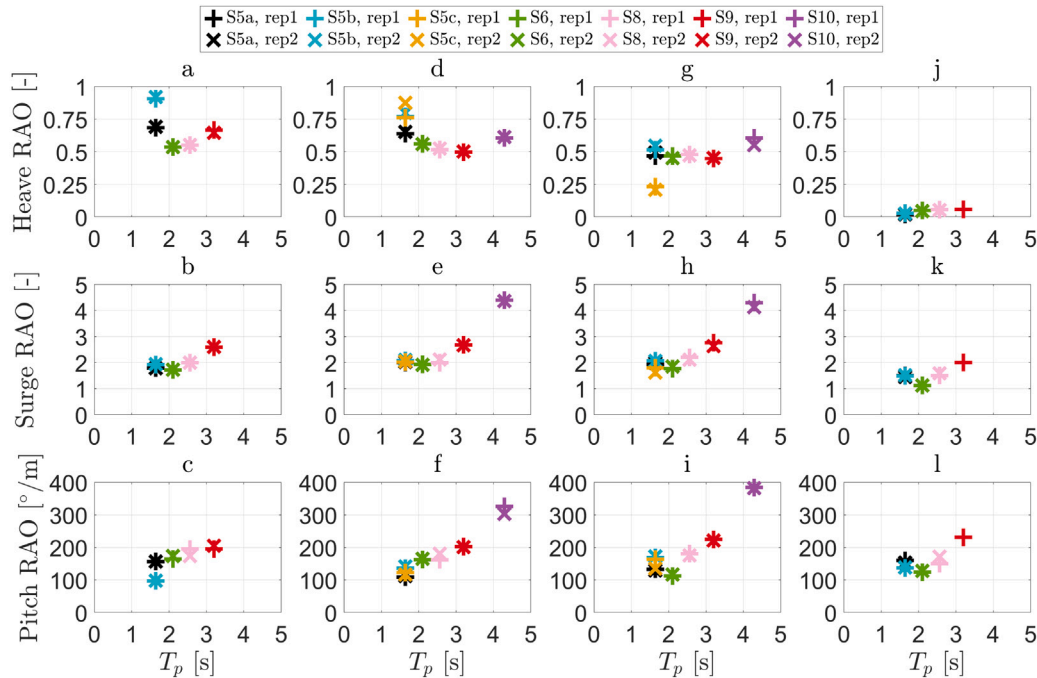


Fig. 27. RAO for focused waves and for all damping cases in heave, surge, and pitch motion. RAO in heave for damping cases of D_0 , D_1 , D_2 , and D_∞ is presented in a, d, g, and j, respectively and is computed as: $RAO_{heave} = \text{maximum heave motion}/\text{maximum surface elevation}$. RAO in surge for damping cases of D_0 , D_1 , D_2 , and D_∞ is presented in b, e, h, and k, respectively and is computed as: $RAO_{surge} = \text{maximum surge motion}/\text{maximum surface elevation}$. RAO in pitch for damping cases of D_0 , D_1 , D_2 , and D_∞ is presented in c, f, i, and l, respectively and is computed as: $RAO_{pitch} = \text{maximum pitch motion}/\text{maximum surface elevation}$.

waves for other sea states and compare the line force results with the irregular and focused waves representations.

In the attempt to minimize the maximum line force of the point absorber in the event of extreme waves, changing the PTO damping can be considered as a strategy. Here, we observe that there exists an optimum damping value for which the structure experiences lower line forces. For irregular waves, see Fig. 12a, the peak of the line force versus damping follows a bathtub trend where the highest peak forces are seen for the upper (infinite) and lower (zero) bound of the PTO damping configuration. At infinite damping coefficient case, i.e. locked PTO, the highest relative velocity between the buoy and water results in a higher hydrodynamic force on the buoy which increases the line force. On the other hand, the WEC has the highest acceleration in zero damping which results in more frequent and harsher compression of the end-stop spring, and thus, higher line force. The influence of the non-linearity such as overtopping is more evident in the focused waves due to their nature of short time duration with one major wave crest, while the irregular waves have more number of large waves leading to more opportunities for high line forces, see Appendix A. Thereby, the same bathtub trend may not be clearly seen for the focused waves, see Fig. 12b.

During the steepest waves in the experiment, clear wave breaking is seen for the irregular waves in sea states 5a and 6 although their breaker index lies below the breaking line presented by Goda, see Fig. 9. This emphasizes the variability of the breaker index (H_b/h) which means that the waves can break even below the breaking line, especially for irregular waves, see Goda (2010). This variability in the breaking index needs to be considered to not underestimate the effect of wave breaking slamming during the analysis.

The peaks in the line force occur mainly during two events of the end-stop spring compression and wave breaking slamming. Out of seven investigated sea states, only sea state 5c ($H_s = 0.07$ m, $T_p = 1.64$ s) has no end-stop spring compression while sea state 10 with the same

wave height but $T_p = 4.29$ s shows clear end-stop involvement. This implies that within the same H_s , longer wave period associates with a longer wavelength and larger surge motion which leads to higher displacement of the PTO translator and thereby more end-stop spring compression. Wave breaking just before the buoy leads to high impact pressure and slamming which induces higher horizontal force compared to non-breaking waves. However, for a point-absorbing device, this event can be accompanied by overtopping which levels out the peak line force. It is worth noting that overtopping may lead to lower line force, and hence, resulting in smaller damage at the connection point at the bottom of the buoy that is considered a critical part in the survivability of the structure. However, other parts of the buoy may experience high forces during this event, and thus, it is important to analyze the overtopping forces acting on the buoy particularly for the systems that the buoy hull contains the PTO and other electrical and mechanical sub-systems.

The heave response of the device shows clear amplification when operating in the waves with frequencies close to the natural frequency of the WEC, see Fig. 27. However, the line force is the result of WEC dynamics in all degrees of freedom. Keeping the wave height constant, smaller wave frequency means longer wavelength which directly affects the surge motion of the buoy, e.g. compare sea states 10 and 5c in Fig. 14. Thereby, in the absence of other non-linear phenomena such as wave breaking slamming, see Section 4.5, operating in waves with smaller frequencies than the natural frequency of the system may lead to higher forces in the line due to more energetic surge motion.

The comparison of the line force in different sea states shown here is not limited to a specific anchoring configuration, although the number of pulleys may affect the friction force of the system. However, the conclusive remarks on this comparison between different sea states and damping configurations are expected to be valid.

6. Conclusions

This paper presents the results of the wave tank experiments for a 1:30 scaled WEC in intermediate water depth with a friction damping linear PTO and a cylindrical buoy with ellipsoidal bottom in extreme sea states with a 50-year return period from the Dowsing site in the North Sea. Five out of the seven selected sea states are along the 50-year contour, and two (5b and 5c) are chosen inside the contour to study the effect of different significant wave heights and peak periods on the line force. Three wave-type representations (irregular, regular, and focused waves) of the same sea state are examined. Four PTO damping cases of $F_{D_0} \approx 0$ N, $F_{D_1} \approx 7.4$ N, $F_{D_2} \approx 18.9$ N, and locked PTO case (infinite damping coefficient) are considered. The PTO includes an upper end-stop spring, and its influence on the dynamics in extreme waves has been analyzed.

The results for the line force show that different wave types do not necessarily give the same peak force. It is illustrated that irregular waves, compared to focused waves, are the most conservative choice in assessing the extreme waves as they show the highest peak force.

If changing the damping is adopted as a strategy for reducing the line force in extreme events, the results suggest that there exists an optimum damping value for which the smallest peak in the line force is obtained. Our results confirm earlier studies (Göteman et al., 2015; Sjökvist et al., 2017) who have seen that a higher PTO damping can be used to reduce peak line forces. However, we extend the previous studies by considering the whole PTO damping configuration range from D_0 to D_∞ where increasing the damping from zero did reduce the peak line force down to a minimum value after which further increase in the damping resulted in a higher peak line force.

Extreme waves include non-linear phenomena such as wave breaking and overtopping. High horizontal (surge) forces are the result of the breaking waves on the device which lead to high line force. Overtopping on the other hand contributes to a reduction of the maximum line force.

Long waves with small wave frequency induce large surge motion on the device which can subsequently increase the line force in the comparison of the sea states with the same significant wave height. An implication of this is that numerical modeling should not be restricted only to heave in order to capture the full dynamics and peak forces in extreme waves. Keeping T_p constant, the significant wave height is proportional to the peak of the line force. In extreme conditions, the effect of non-linear phenomena must also be taken into account as it was discussed extensively in Section 4.

The compression of the end-stop spring is more frequent in lower damping cases and is the main cause for the peaks of the line force.

CRedit authorship contribution statement

Zahra Shahroozi: Designed and conducted the experiments, Analyzed the data, Wrote the paper. **Malin Göteman:** Supervised the work, Discussed the results, Edited the paper, Acquired the funding for the project. **Jens Engström:** Supervised the work, Discussed the results, Edited the paper, Acquired the funding for the project.

Declaration of competing interest

The authors declare that they have no known competing financial interests or personal relationships that could have appeared to influence the work reported in this paper.

Appendix A. Comparison of the line force for different wave types

See Figs. 28–34.

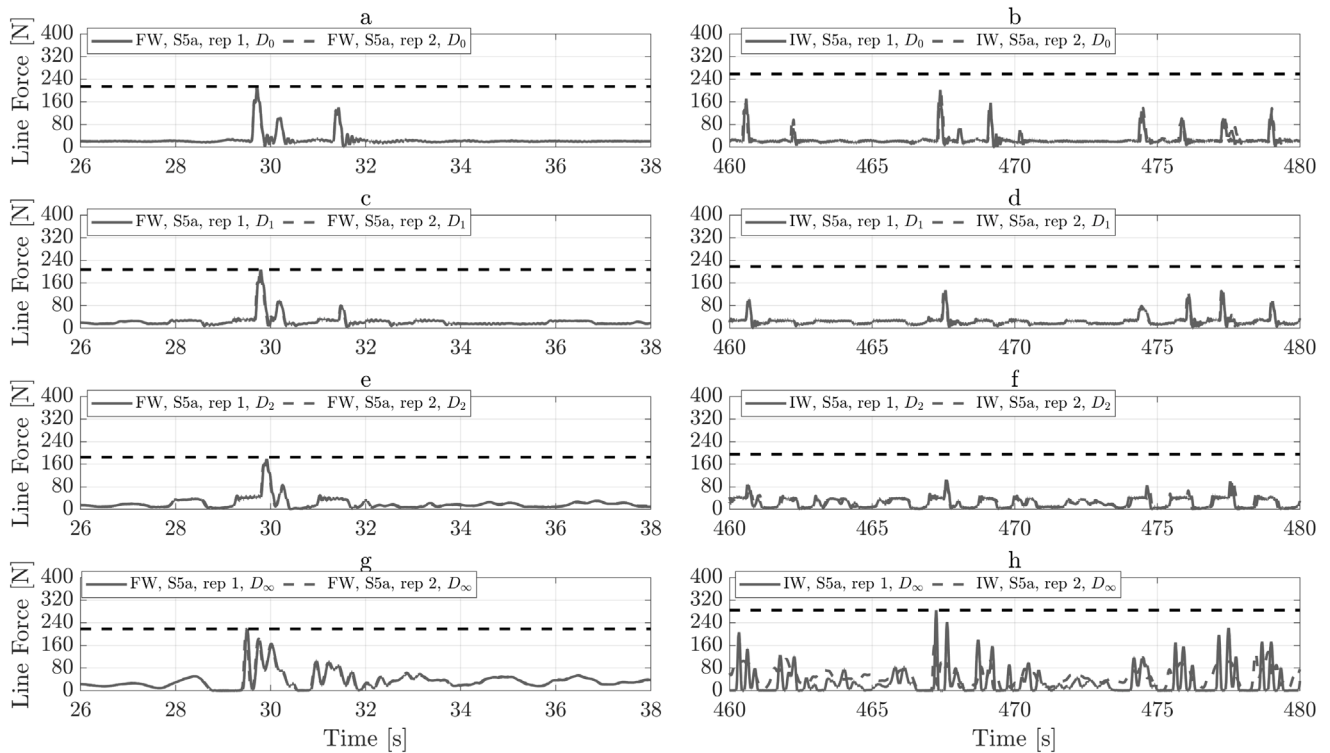


Fig. 28. Comparison of the line force for different wave types for sea state 5a, where a, c, e, and g are focused waves while b, d, f, and h are irregular waves for D_0 , D_1 , D_2 , and D_∞ . The dashed lines represent the maximum line force for the entire period of the experiment in each wave type.

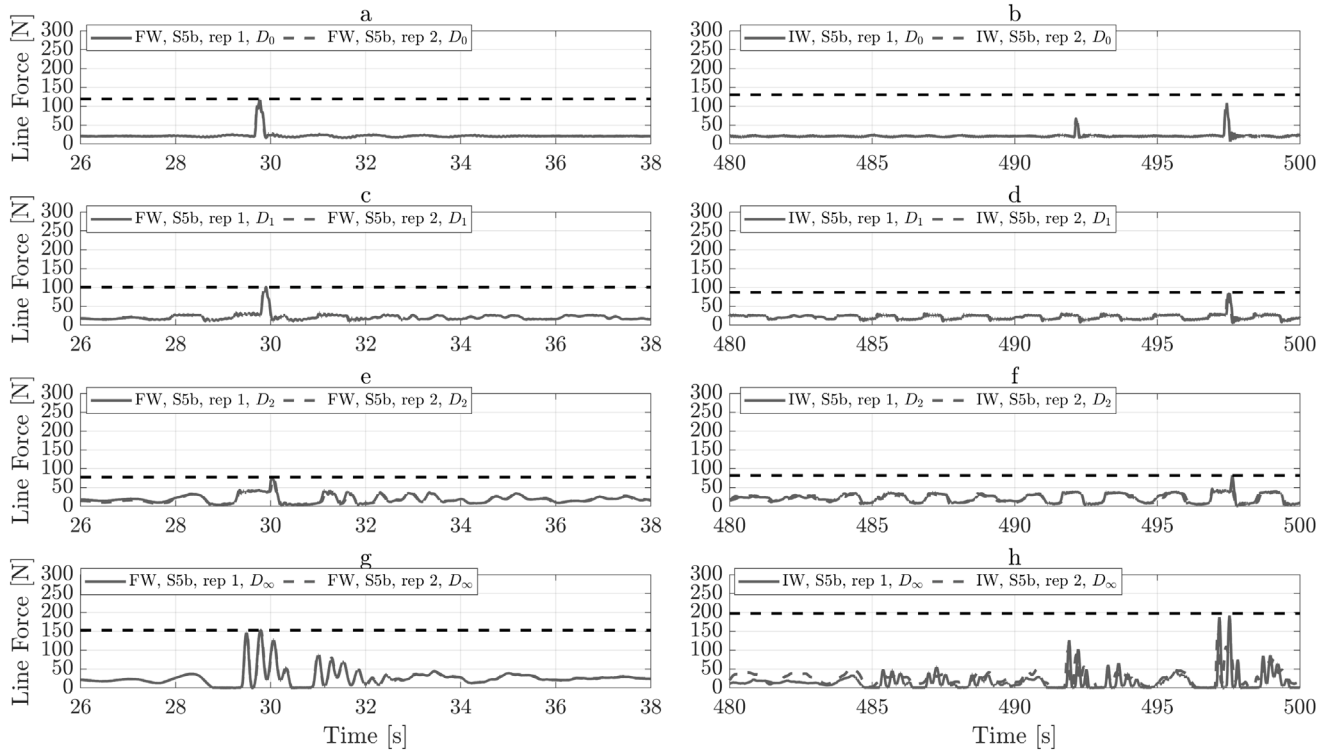


Fig. 29. Comparison of the line force for different wave types for sea state 5b, where *a*, *c*, *e*, and *g* are focused waves while *b*, *d*, *f*, and *h* are irregular waves for D_0 , D_1 , D_2 , and D_∞ . The dashed lines represent the maximum line force for the entire period of the experiment in each wave type.

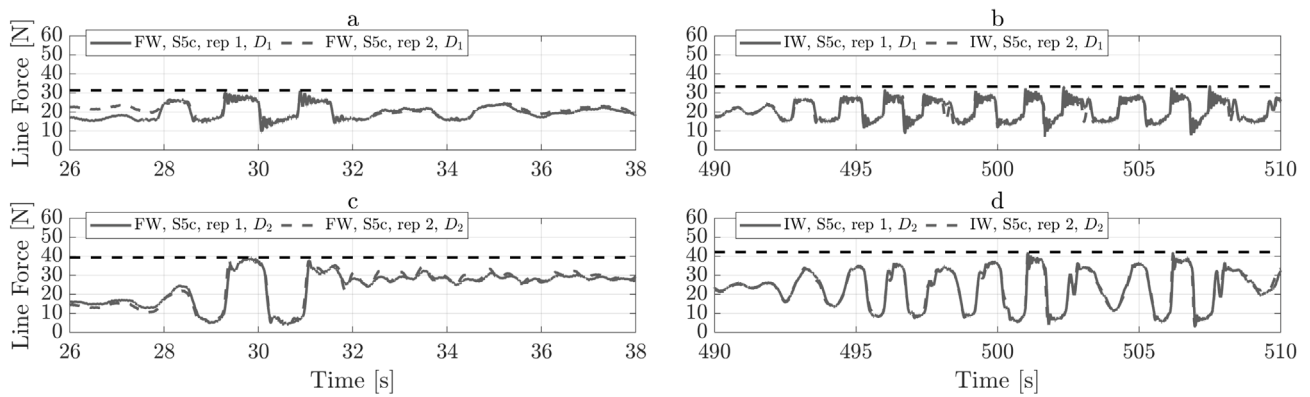


Fig. 30. Comparison of the line force for different wave types for sea state 5c, where *a* and *c* are focused waves, and *b* and *d* are irregular waves for D_1 and D_2 . The dashed lines represent the maximum line force for the entire period of the experiment in each wave type.

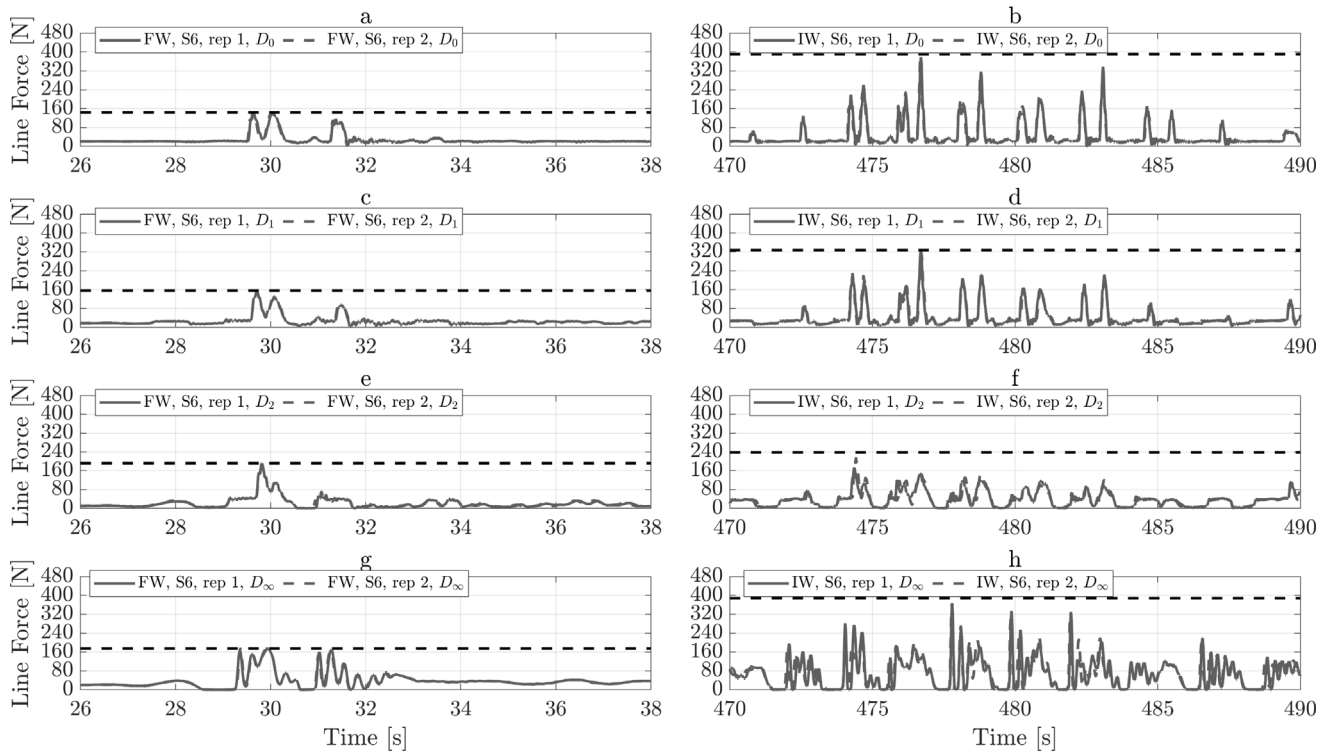


Fig. 31. Comparison of the line force for different wave types for sea state 6, where *a*, *c*, *e*, and *g* are focused waves while *b*, *d*, *f*, and *h* are irregular waves for D_0 , D_1 , D_2 , and D_∞ . The dashed lines represent the maximum line force for the entire period of the experiment in each wave type.

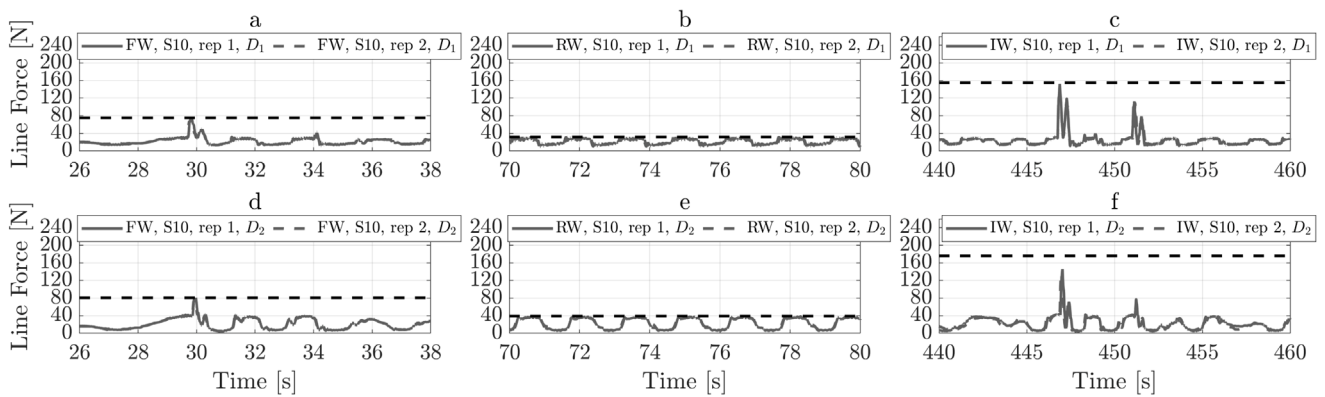


Fig. 32. Comparison of the line force for sea state 10, where *a* and *d* are focused waves, *b* and *e* are regular waves, and *c* and *f* are irregular waves for D_1 and D_2 . The dashed lines represent the maximum line force for the entire period of the experiment.

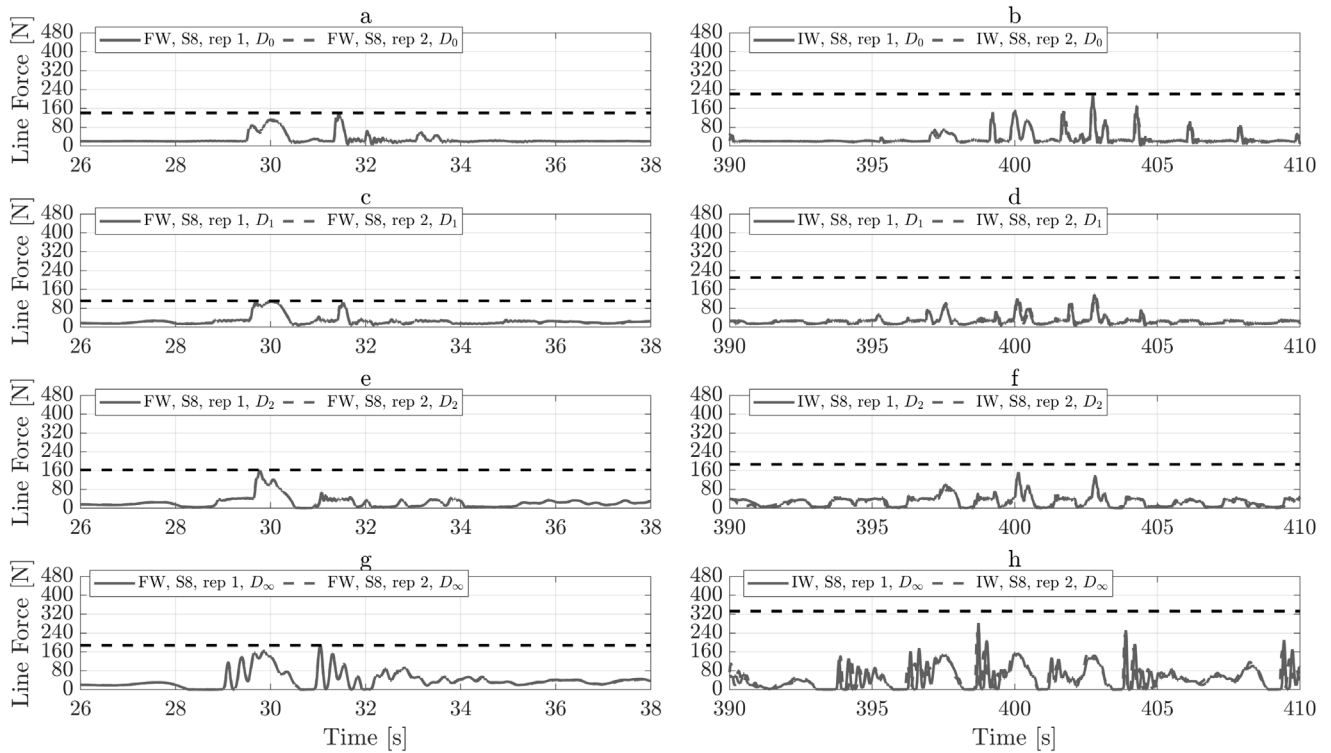


Fig. 33. Comparison of the line force for different wave types for sea state 8, where a, c, e, and g are focused waves while b, d, f, and h are irregular waves for D_0 , D_1 , D_2 , and D_∞ . The dashed lines represent the maximum line force for the entire period of the experiment in each wave type.

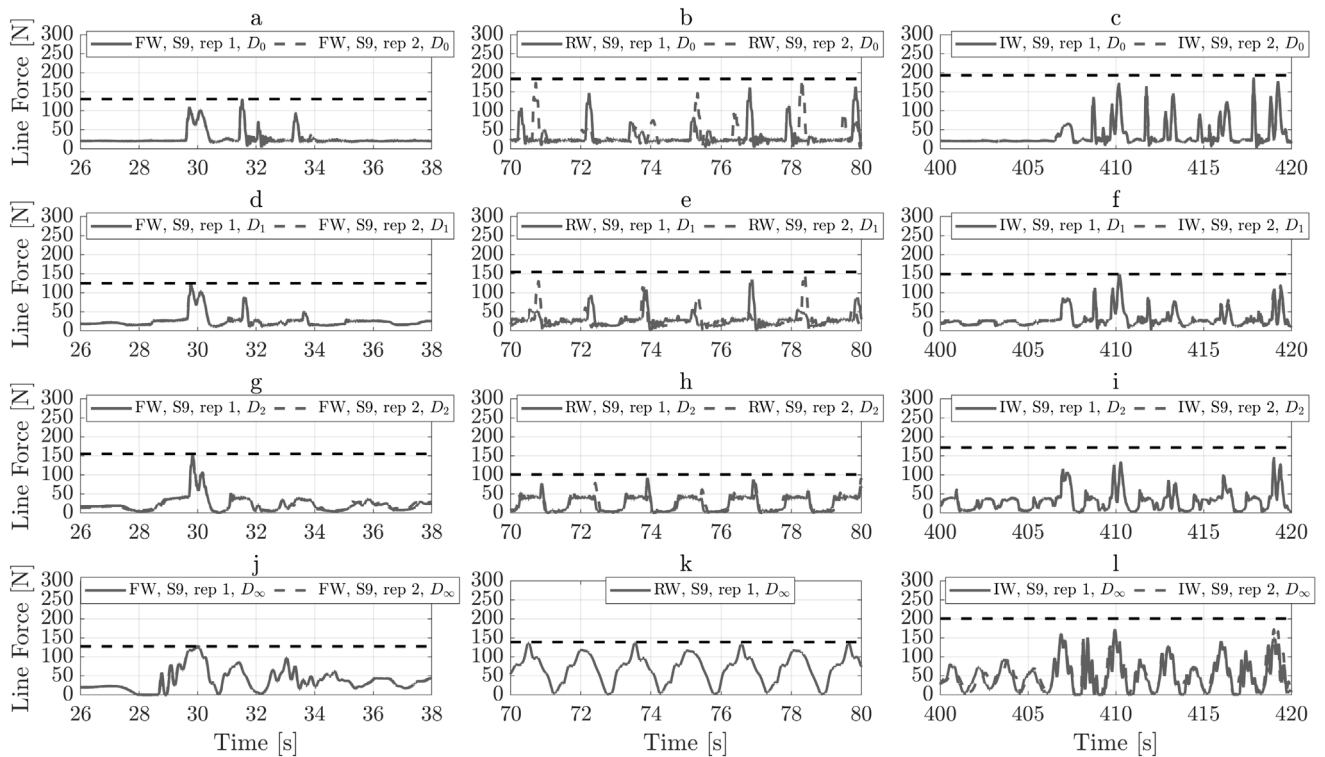


Fig. 34. Comparison of the line force for different wave types for sea state 9, where a, d, g, and j are focused waves, b, e, h and k are regular waves, and c, f, i, and l are irregular waves for D_1 and D_2 . The dashed lines represent the maximum line force for the entire period of the experiment in each wave type.

Appendix B. Motion and line force

See Figs. 35–38.

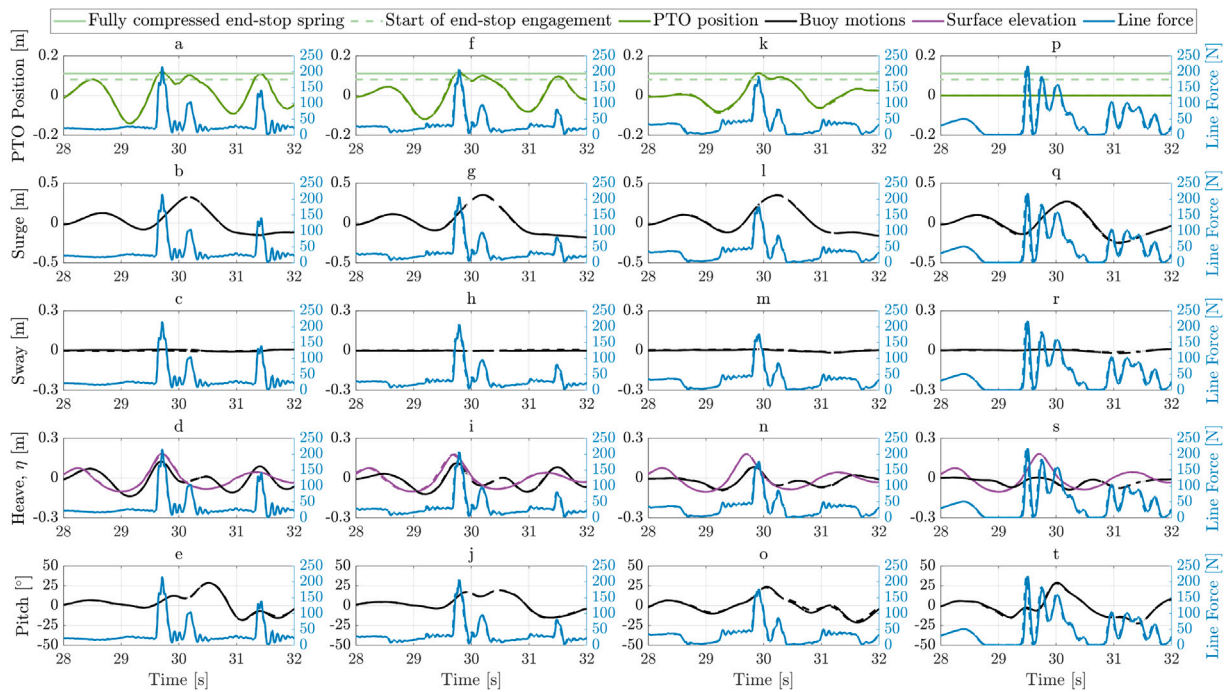


Fig. 35. Buoy's motions and line force in focused waves for sea state 5a where $a, b, c, d,$ and e represent damping D_0 ; $f, g, h, i,$ and j represent D_1 ; $k, l, m, n,$ and o represent D_2 ; $p, q, r, s,$ and t represent D_∞ . The surface elevation is η .

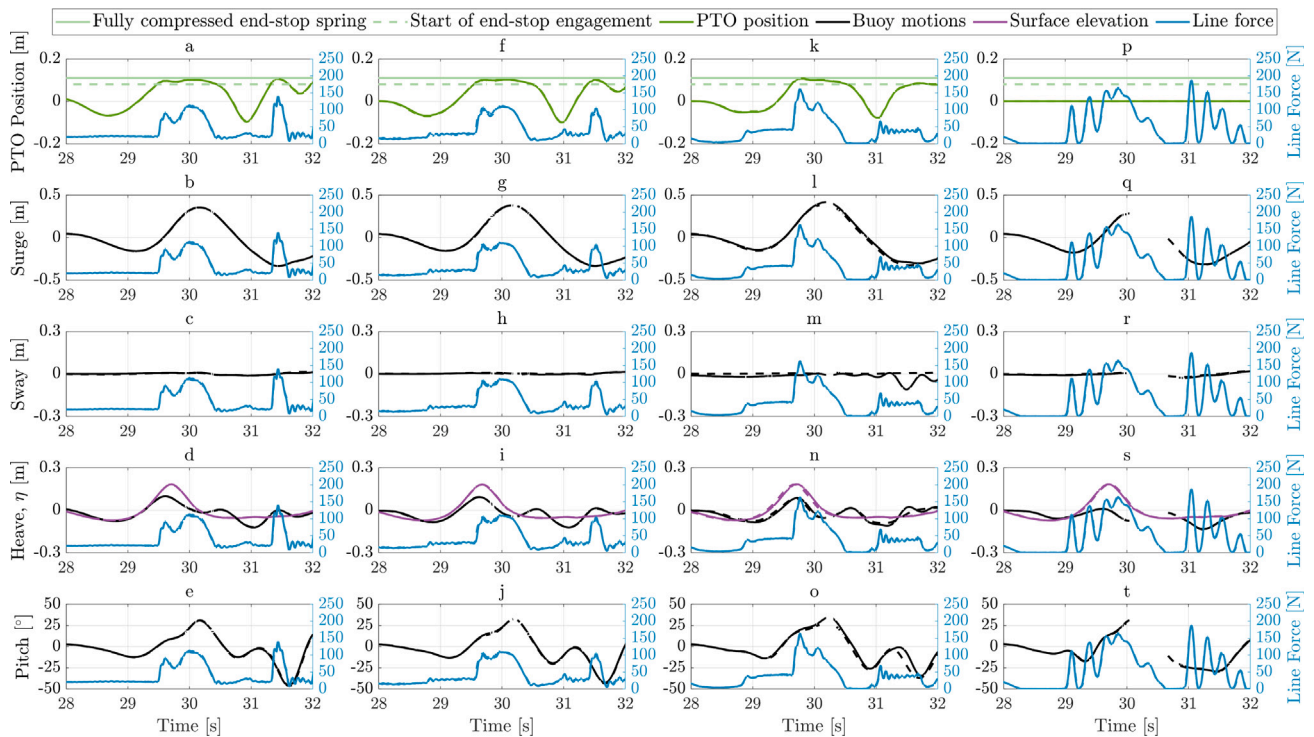


Fig. 36. Buoy's motions and line force in focused waves for sea state 8 where $a, b, c, d,$ and e represent damping D_0 ; $f, g, h, i,$ and j represent D_1 ; $k, l, m, n,$ and o represent D_2 ; $p, q, r, s,$ and t represent D_∞ . The surface elevation is η .

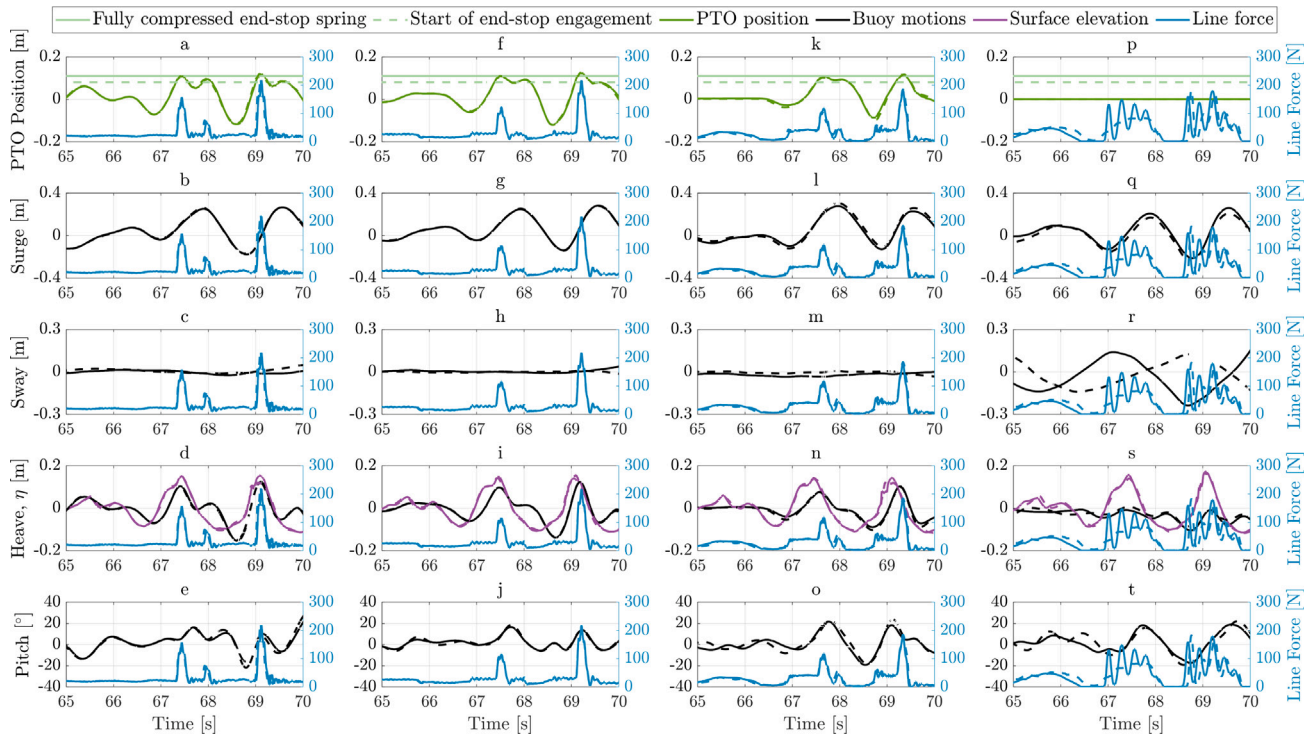


Fig. 37. Buoy's motion and line force in **irregular waves** for a few seconds in sea state 5a where a, b, c, d, and e represent damping D_0 ; f, g, h, i, and j represent D_1 ; k, l, m, n, and o represent D_2 ; p, q, r, s, and t represent D_∞ . The surface elevation is η .

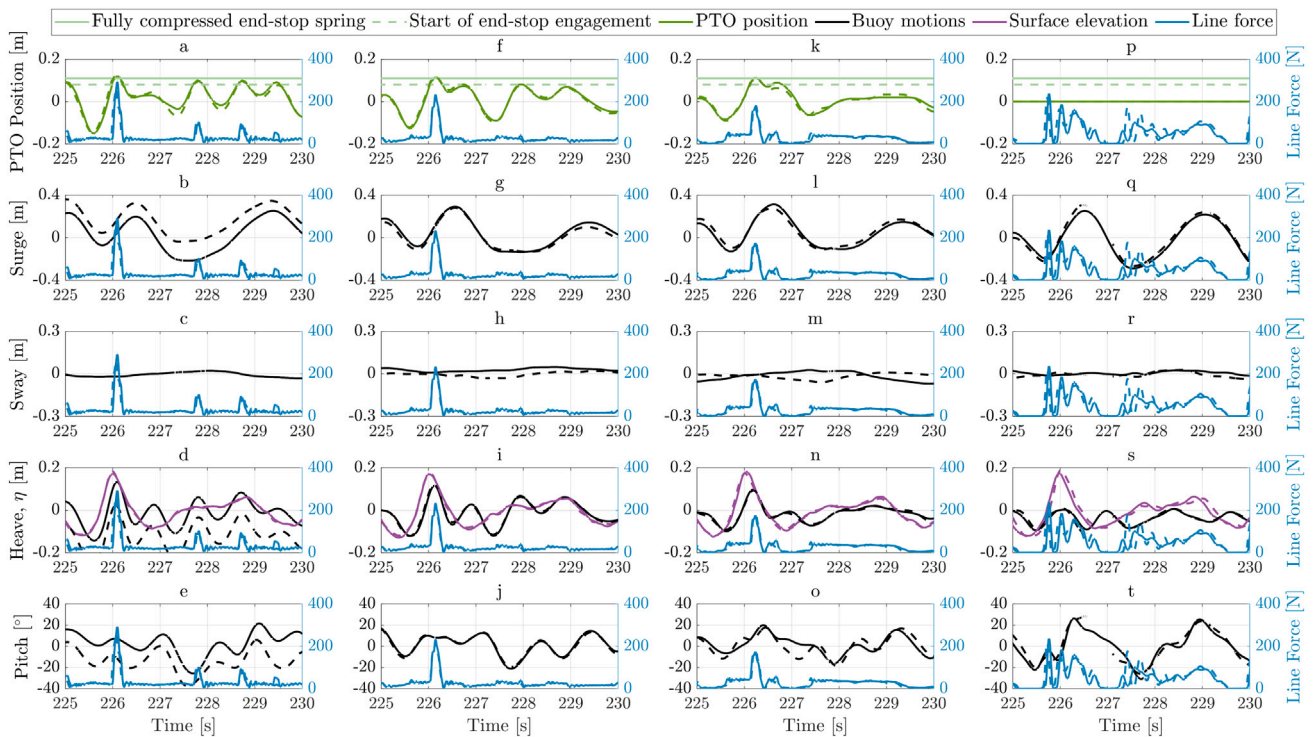


Fig. 38. Buoy's motion and line force in **irregular waves** for a few seconds in sea state 6 where a, b, c, d, and e represent damping D_0 ; f, g, h, i, and j represent D_1 ; k, l, m, n, and o represent D_2 ; p, q, r, s, and t represent D_∞ . The surface elevation is η .

References

- Aalborg-University, 2020. Hydraulic-and-coastal-engineering-laboratory. https://www.en.build.aau.dk/digitalAssets/823/823791_hydraulic-and-coastal-engineering-laboratory-12-05-2020.pdf.
- Askar, H., Lo, J., Hamadeh, R., Tayfun, M., 1995. Distribution of wave steepness. *J. Univ. Kuwait (Sci.)* 22 (2), 155–165.
- Balachandran, B., Magrab, E.B., 2018. *Vibrations*. Cambridge University Press.
- Chakrabarti, S.K., 1987. *Hydrodynamics of Offshore Structures*. WIT Press.
- Clauss, G.F., Bergmann, J., 1986. Gaussian wave packets—a new approach to seakeeping testsof ocean structures. *Appl. Ocean Res.* 8 (4), 190–206.
- Coe, R.G., Neary, V.S., et al., 2014. Review of methods for modeling wave energy converter survival in extreme sea states.
- Cokelet, E., 1977. Breaking waves. *Nature* 267 (5614), 769–774.
- De Backer, G., Vantorre, M., Beels, C., De Pré, J., Victor, S., De Rouck, J., Blommaert, C., Van Paeppegem, W., 2009. Experimental investigation of water impact on axisymmetric bodies. *Appl. Ocean Res.* 31 (3), 143–156.
- De Backer, G., Vantorre, M., Frigaard, P., Beels, C., De Rouck, J., 2010. Bottom slamming on heaving point absorber wave energy devices. *J. Mar. Sci. Technol.* 15 (2), 119–130.
- De Backer, G., Vantorre, M., Victor, S., De Rouck, J., Beels, C., 2008. Investigation of vertical slamming on point absorbers. In: *International Conference on Offshore Mechanics and Arctic Engineering*, Vol. 48234. pp. 851–859.
- Falnes, J., Kurmiawan, A., 2020. *Ocean Waves and Oscillating Systems: Linear Interactions Including Wave-Energy Extraction*, Vol. 8. Cambridge University Press.
- Goda, Y., 2010. Reanalysis of regular and random breaking wave statistics. *Coast. Eng.* 52 (1), 71–106.
- Götteman, M., Engström, J., Eriksson, M., Hann, M., Ransley, E., Greaves, D., Leijon, M., 2015. Wave loads on a point-absorbing wave energy device in extreme waves. In: *The Twenty-Fifth International Ocean and Polar Engineering Conference*. OnePetro.
- Hann, M., Greaves, D., Raby, A., 2015. Snatch loading of a single taut moored floating wave energy converter due to focussed wave groups. *Ocean Eng.* 96, 258–271.
- Kapsenberg, G.K., 2018. On the slamming of ships: Development of an approximate slamming prediction method.
- Katsidoniotaki, E., Nilsson, E., Rutgersson, A., Engström, J., Götteman, M., 2021. Response of point-absorbing wave energy conversion system in 50-years return period extreme focused waves. *J. Mar. Sci. Eng.* 9 (3), 345.
- Katsidoniotaki, E., Ransley, E., Brown, S., Palm, J., Engström, J., Götteman, M., 2020. Loads on a point-absorber wave energy converter in regular and focused extreme wave events. In: *ASME 2020 39th International Conference on Ocean, Offshore and Arctic Engineering*. American Society of Mechanical Engineers Digital Collection.
- Kofoed, J.P., 2002. Wave overtopping of marine structures: utilization of wave energy.
- Liu, Y., Niu, X., Yu, X., 2011. A new predictive formula for inception of regular wave breaking. *Coast. Eng.* 58 (9), 877–889.
- McCowan, J., 1894. XXXIX. ON the highest wave of permanent type. *Lond. Edinb. Dublin Philos. Mag. J. Sci.* 38 (233), 351–358.
- Miche, M., 1944. Mouvements ondulatoires de la mer en profondeur constante ou décroissante. *Ann. Ponts Chaussées* pp (1) 26-78, (2) 270-292, (3) 369-406.
- Molland, A.F., 2011. *The Maritime Engineering Reference Book: A Guide To Ship Design, Construction and Operation*, Chapter 7 - Seakeeping. Elsevier.
- Munk, W.H., 1949. The solitary wave theory and its application to surf problems. *Ann. New York Acad. Sci.* 51 (3), 376–424.
- Ning, D., Zang, J., Liu, S., Taylor, R.E., Teng, B., Taylor, P., 2009. Free-surface evolution and wave kinematics for nonlinear uni-directional focused wave groups. *Ocean Eng.* 36 (15–16), 1226–1243.
- Pecher, A., Kofoed, J.P., 2017. Erratum to: *Handbook of ocean wave energy*. In: *Handbook of Ocean Wave Energy*. Springer, p. E1.
- Qualisys, 2021. *The qualisys motion capture system*. <https://www.qualisys.com>.
- Rafiee, A., Fiévez, J., 2015. Numerical prediction of extreme loads on the CETO wave energy converter. In: *Proceedings of the 11th European Wave and Tidal Energy Conference*. Nantes, France no. 09A1-2.
- Ransley, E., Greaves, D., Raby, A., Simmonds, D., Hann, M., 2017. Survivability of wave energy converters using CFD. *Renew. Energy* 109, 235–247.
- van Rij, J.A., Yu, Y.-H., Tom, N.M., 2019. Validation of Simulated Wave Energy Converter Responses to Focused Waves for CCP-WSI Blind Test Series 2. Tech. rep., National Renewable Energy Lab.(NREL), Golden, CO (United States).
- Ropero-Giralda, P., Crespo, A.J., Tagliaferro, B., Altomare, C., Domínguez, J.M., Gómez-Gesteira, M., Viccione, G., 2020. Efficiency and survivability analysis of a point-absorber wave energy converter using DualSPHysics. *Renew. Energy* 162, 1763–1776.
- Rue, H., 1993. Joint distribution of successive wave steepness parameters. *J. Offshore Mech. Arct. Eng.* 115, 191.
- Saincher, S., Banerjee, J., 2016. Influence of wave breaking on the hydrodynamics of wave energy converters: A review. *Renew. Sustain. Energy Rev.* 58, 704–717.
- Salaudinn, M., Pearson, J., 2020. Laboratory investigation of overtopping at a sloping structure with permeable shingle foreshore. *Ocean Eng.* 197, 106866.
- Sawaragi, T., 1995. *Coastal Engineering-Waves, Beaches, Wave-Structure Interactions*. Elsevier, (Chapter 2).
- Shahroozi, Z., 2021. *Prediction Horizon Requirement in Control and Extreme Load Analyses for Survivability: Advancements to Improve the Performance of Wave Energy Technologies* (Ph.D. thesis). Uppsala University.
- Shahroozi, Z., Götteman, M., Engström, J., 2021. Experimental results of force measurements from a scaled point absorbing wave energy converter subjected to extreme waves. In: Greaves, D. (Ed.), *Proceedings of the Fourteenth European Wave and Tidal Energy Conference*. EWTEC, University of Plymouth, UK, pp. 1881–1–1881-10 , ISSN: 2309-1983.
- Sjökqvist, L., Wu, J., Ransley, E., Engström, J., Eriksson, M., Götteman, M., 2017. Numerical models for the motion and forces of point-absorbing wave energy converters in extreme waves. *Ocean Eng.* 145, 1–14.
- Tayfun, M.A., 2006. Distributions of wave steepness and surf parameter. *J. Waterw. Port Coast. Ocean Eng.* 132 (1), 1–9.
- Toffoli, A., Babanin, A., Onorato, M., Waseda, T., 2010. Maximum steepness of oceanic waves: Field and laboratory experiments. *Geophys. Res. Lett.* 37 (5).
- Tromans, P.S., Anaturk, A.R., Hagemeijer, P., et al., 1991. A new model for the kinematics of large ocean waves-application as a design wave. In: *The First International Offshore and Polar Engineering Conference*. International Society of Offshore and Polar Engineers.
- Veritas, D.N., 2010. *Recommended practice dnv-rp-c205: environmental conditions and environmental loads*. DNV, Norway.
- Von Karman, T., 1929. The impact on seaplane floats during landing.
- Wagner, H., 1932. Über stoß -und gleitvorgänge an der oberfläche von flüssigkeiten. *ZAMM-J. Appl. Math. Mech./Z. Angew. Math. Mech.* 12 (4), 193–215.
- Wang, S., Soares, C.G., 2017. Review of ship slamming loads and responses. *J. Mar. Sci. Appl.* 16 (4), 427–445.
- Wienke, J., Sparboom, U., Oumeraci, H., 2001. Breaking wave impact on a slender cylinder. In: *Coastal Engineering 2000*. pp. 1787–1798.
- Wrang, L., Katsidoniotaki, E., Nilsson, E., Rutgersson, A., Rydén, J., Götteman, M., 2021. Comparative analysis of environmental contour approaches to estimating extreme waves for offshore installations for the baltic sea and the north sea. *J. Mar. Sci. Eng.* 9 (1), 96.
- Yamada, H., Shiotani, T., 1968. On the highest water waves of permanent type. *Bull. Disaster Prev. Res. Inst.* 18 (2), 1–22.
- Yu, Y.-H., Van Rij, J., Coe, R., Lawson, M., 2015. Preliminary wave energy converters extreme load analysis. In: *ASME 2015 34th International Conference on Ocean, Offshore and Arctic Engineering*. American Society of Mechanical Engineers Digital Collection.